



Imaging of I Zw 18 by JWST. I. Detecting Dusty Stellar Populations

Downloaded from: <https://research.chalmers.se>, 2025-07-01 00:02 UTC

Citation for the original published paper (version of record):

Hirschauer, A., Crouzet, N., Habel, N. et al (2024). Imaging of I Zw 18 by JWST. I. Detecting Dusty Stellar Populations. *Astronomical Journal*, 168(1). <http://dx.doi.org/10.3847/1538-3881/ad4967>

N.B. When citing this work, cite the original published paper.



Imaging of IZw 18 by JWST. I. Detecting Dusty Stellar Populations

Alec S. Hirschauer¹, Nicolas Crouzet², Nolan Habel³, Laura Lenkić^{3,4}, Conor Nally⁵, Olivia C. Jones⁶, Giacomo Bortolini⁷, Martha L. Boyer¹, Kay Justtanont⁸, Margaret Meixner³, Göran Östlin⁷, Gillian S. Wright⁶, Ruyman Azzollini⁹, Joris A. D. L. Blommaert¹⁰, Bernhard Brandl², Leen Decin¹¹, Ommarayani Nayak^{1,12}, Pierre Royer¹¹, B. A. Sargent^{1,13}, and Paul van der Werf²

¹ Space Telescope Science Institute, 3700 San Martin Drive, Baltimore, MD 21218, USA; ahirschauer@stsci.edu

² Leiden Observatory, Leiden University, P.O. Box 9513, 2300 RA Leiden, The Netherlands

³ Jet Propulsion Laboratory, California Institute of Technology, 4800 Oak Grove Drive, Pasadena, CA 91109, USA

⁴ Stratospheric Observatory for Infrared Astronomy, NASA Ames Research Center, Mail Stop 204-14, Moffett Field, CA 94035, USA

⁵ Institute for Astronomy, University of Edinburgh, Blackford Hill, Edinburgh, EH9 3HJ, UK

⁶ UK Astronomy Technology Centre, Royal Observatory, Blackford Hill, Edinburgh, EH9 3HJ, UK

⁷ The Oskar Klein Centre, Department of Astronomy, Stockholm University, AlbaNova, SE-10691 Stockholm, Sweden

⁸ Chalmers University of Technology, Dept. Space, Earth and Environment, Onsala Space Observatory, 439 92 Onsala, Sweden

⁹ Mullard Space Science Laboratory, University College London, Holmbury St Mary, Dorking, Surrey, RH5 6NT, UK

¹⁰ Astronomy and Astrophysics Research Group, Department of Physics and Astrophysics, VU Brussel, Pleinlaan 2, B-1050 Brussels, Belgium

¹¹ Instituut voor Sterrenkunde, KU Leuven, Celestijnenlaan 200D, 3001 Leuven, Belgium

¹² NASA Goddard Space Flight Center, 8800 Greenbelt Road, Greenbelt, MD 20771, USA

¹³ Department of Physics & Astronomy, Johns Hopkins University, 3400 N. Charles Street, Baltimore, MD 21218, USA

Received 2024 February 16; revised 2024 April 25; accepted 2024 May 7; published 2024 June 21

Abstract

We present a JWST imaging survey of IZw 18, the archetypal extremely metal-poor, star-forming (SF), blue compact dwarf galaxy. With an oxygen abundance of only $\sim 3\% Z_{\odot}$, it is among the lowest-metallicity systems known in the local Universe, and is, therefore, an excellent accessible analog for the galactic building blocks which existed at early epochs of ionization and star formation. These JWST data provide a comprehensive infrared (IR) view of IZw 18 with eight filters utilizing both Near Infrared Camera (F115W, F200W, F356W, and F444W) and Mid-Infrared Instrument (F770W, F1000W, F1500W, and F1800W) photometry, which we have used to identify key stellar populations that are bright in the near- and mid-IR. These data allow for a better understanding of the origins of dust and dust-production mechanisms in metal-poor environments by characterizing the population of massive, evolved stars in the red supergiant (RSG) and asymptotic giant branch (AGB) phases. In addition, it enables the identification of the brightest dust-enshrouded young stellar objects (YSOs), which provide insight into the formation of massive stars at extremely low metallicities typical of the very early Universe. This paper provides an overview of the observational strategy and data processing, and presents first science results, including identifications of dusty AGB, RSG, and bright YSO candidates. These first results assess the scientific quality of JWST data and provide a guide for obtaining and interpreting future observations of the dusty and evolved stars inhabiting compact dwarf SF galaxies in the local Universe.

Unified Astronomy Thesaurus concepts: [Stellar populations \(1622\)](#); [Evolved stars \(481\)](#); [Asymptotic giant branch stars \(2100\)](#); [Red supergiant stars \(1375\)](#); [Dust formation \(2269\)](#); [Dwarf irregular galaxies \(417\)](#); [Blue compact dwarf galaxies \(165\)](#); [James Webb Space Telescope \(2291\)](#); [Infrared astronomy \(786\)](#); [Infrared photometry \(792\)](#)

1. Introduction

Metal-poor star-forming (SF) dwarf galaxies in the local Universe represent accessible analogs to those at high redshift (e.g., Motiño Flores et al. 2021). As the enrichment history for a given system traces the buildup of heavy elements from successive generations of stellar nucleosynthesis, a low-abundance galaxy mimics the astrophysical conditions common in the early Universe, including the universal epoch of peak star formation (“cosmic noon,” $z \sim 1.5$ – 2 ; Madau & Dickinson 2014; Van Sistine et al. 2016), at which point a majority of the Universe’s star formation and chemical enrichment is expected to have taken place. At the very lowest metallicities, we may therefore approximate the SF environments of the time period shortly after the Big Bang. IZw 18 is

among the most extremely metal-poor (XMP; $Z < 0.1 Z_{\odot}$) systems known ($12 + \log(\text{O}/\text{H}) = 7.17 \pm 0.04$), with a measured gas-phase oxygen abundance of only approximately 3% solar (e.g., Alloin et al. 1979; Lequeux et al. 1979; French 1980; Kinman & Davidson 1981; Pagel et al. 1992; Skillman & Kennicutt 1993; Izotov et al. 1999; Leboutteiller et al. 2013). At a distance of 18.2 ± 1.5 Mpc (Aloisi et al. 2007) and with global star formation rate (SFR) values measured at $\sim 0.13 M_{\odot} \text{ yr}^{-1}$ (computed via H I absorption; Leboutteiller et al. 2013) to $\sim 0.17 M_{\odot} \text{ yr}^{-1}$ (estimated from radio free-free continuum emission; Hunt et al. 2005), with localized values as high as $\sim 1 M_{\odot} \text{ yr}^{-1}$ (via statistical analysis; Annibali et al. 2013), it is an ideal laboratory for study of both the young and evolved star demographics in an environment analogous to that found in the very early Universe. Typical of such systems, IZw 18 has an enhanced total X-ray luminosity per unit of SFR (Leboutteiller et al. 2017). Additional properties of IZw 18 are listed in Table 1.

As the archetypal blue compact dwarf (BCD) galaxy, IZw 18 is currently experiencing a period of intensely elevated



Original content from this work may be used under the terms of the [Creative Commons Attribution 4.0 licence](#). Any further distribution of this work must maintain attribution to the author(s) and the title of the work, journal citation and DOI.

Table 1
Properties of I Zw 18

Observed Global Quantities	Value	Reference
R.A. (J2000)	09:34:02	Izotov & Thuan (2016)
Decl. (J2000)	+55:14:28	Izotov & Thuan (2016)
Distance	18.2 ± 1.5 Mpc	Aloisi et al. (2007)
Distance modulus	31.30 ± 0.17	Aloisi et al. (2007)
Recessional velocity	751 ± 2 km s ⁻¹	Thuan et al. (1999)
Redshift	0.00251	Izotov & Thuan (2016)
Stellar mass (M_*)	$2.0 \times 10^7 M_\odot$	Madden et al. (2014)
Gas mass (H I)	$1.0 \times 10^8 M_\odot$	Lelli et al. (2012)
Dust mass	$1.1 \times 10^4 M_\odot$	Herrera-Camus et al. (2012)
Extinction (A_V)	0–0.2 mag	Izotov & Thuan (2016)
SFR	$\sim 0.1 - \sim 1 M_\odot \text{ yr}^{-1}$	Lebouteiller et al. (2013); Annibali et al. (2013)
SFR/ M_* (sSFR)	$10^{-7} - 10^{-8} \text{ yr}^{-1}$	A. Aloisi (2024, private communication)
$12 + \log(\text{O}/\text{H})$	7.17 ± 0.04	Skillman & Kennicutt (1993)
$U - B$	-0.88	van Zee et al. (1998)
$B - V$	-0.03	van Zee et al. (1998)

SFR (Janowiecki & Salzer 2014; Janowiecki et al. 2017) and has thus been the subject of focused observations since its discovery (Zwicky 1966; Sargent & Searle 1970; Searle & Sargent 1972). Early descriptions of this system identified two bright regions of star formation separated by $5''.8$ which constitute the main body, subsequently referred to as the northwest (NW) and southeast (SE) components. Active star formation in the brighter NW component was established via observations tracing ionized gas emission (e.g., Hunter & Thronson 1995) and Wolf-Rayet stars (e.g., Izotov et al. 1997; Legrand et al. 1997; de Mello et al. 1998; Brown et al. 2002). This region has an H I envelope which contains inherently metal-free gas pockets (Lebouteiller et al. 2013) among inhomogeneities of the multiphase interstellar medium (ISM; James et al. 2014). An additional diffuse SF region $\sim 22''$ NW of the main body (known as Component C) was identified later (Davidson et al. 1989; Dufour & Hester 1990), with radial velocity studies of the ionized and neutral (H I) gas demonstrating its physical association and common H I envelope with I Zw 18, respectively (e.g., Dufour et al. 1996; Izotov & Thuan 1998; van Zee et al. 1998).

I Zw 18 has been intensely targeted by the Hubble Space Telescope (HST), and while initial studies found no evidence for an old, existing stellar population (e.g., Hunter & Thronson 1995), subsequent work utilizing deeper data confirmed the presence of an early star formation episode based on evidence of asymptotic giant branch (AGB) stars (Aloisi et al. 1999) and gas-phase abundance study (Garnett et al. 1997). Details concerning an intense, recent bout of star formation which began at least ~ 30 – 50 Myr ago were published by Dufour et al. (1996), with the near-infrared (near-IR) study of Östlin (2000) concluding that the stellar population of I Zw 18 is made up of a younger population of red supergiants (RSGs) and an older population of AGB stars, also found by Izotov & Thuan (2004). Subsequent study of these evolved stars by Östlin & Mouhcine (2005) employed HST medium-band filters to additionally identify a subset of five AGB stars via C_2 absorption. The underlying stellar population of Component C was found to be similarly old,

while exhibiting some moderate recent activity (Aloisi et al. 1999; Izotov & Thuan 2004; Jamet et al. 2010).

Establishing a census of evolved stars in I Zw 18 will help to provide for a better understanding of the origins and role of interstellar dust at the earliest epoch of our Universe. While supernovae (SNe) have been found to quickly produce dust in significant quantities locally, it is unclear how similarly this mechanic behaves at the extremely low levels of metal enrichment which characterized galaxies at high redshift. In addition, the rate of both new and existing dust destruction by SNe via the passage of shocks may rival the rate of creation (Temim et al. 2015)! AGB stars are known to be a major source of dust production within nearby systems (e.g., Matsuura et al. 2009). As they evolve, thermal pulsations and convective cell activity push the products of nucleosynthetic reactions from the internal regions previously exposed to helium-burning reactions toward the stellar surface (e.g., Iben 1974, 1975; Lattanzio 1987, 1993; Boothroyd & Sackmann 1988), where its ejection enriches the surrounding ISM. Because AGB stars represent the final evolutionary stage for the vast majority of stars which have left the main sequence (MS), their contributions of dust and heavy elements to the ISM due to mass loss, and the subsequent evolutionary effects on the ISM and other stars, is significant (Höfner & Olofsson 2018).

In metal-poor environments and at high redshift, the dust contribution from these AGB stars is currently not well defined. For ancient galaxies populating the early Universe, the prevailing expectation had been that their low- to intermediate-mass MS progenitor stars would have required a greater amount of time than had presently elapsed in order to evolve to the AGB phase, suggesting that they cannot contribute significantly to the overall dust budget. Recent work, however, has begun casting doubt on this conventional wisdom, with evidence for such evolved stars in the low-metallicity galaxy Sextans A suggesting that these stars could contribute dust at early epochs. Additionally, observational evidence for large reservoirs of dust existing at redshifts up to $z \sim 6$ has been found (Bertoldi et al. 2003; Robson et al. 2004; Beelen et al. 2006; Algera et al. 2023), and perhaps even as distant as $z > 10$ (Curtis-Lake et al. 2023). Furthermore, studies of nearby low-abundance systems such as dwarf galaxies and globular clusters have shown that these environments possess dust originating from evolved stars (McDonald et al. 2010; Whitelock et al. 2018; Jones et al. 2018); however, the effects of metallicity on AGB star dust production are disputed (van Loon et al. 2005; McDonald et al. 2011; Sloan et al. 2012, 2016; Dell’Agli et al. 2019b).

Observational efforts in the IR searching for metal-poor local galaxies possessing populations of evolved stars are ongoing. Prior to the advent of JWST, the state of the art for resolved extragalactic stellar populations was the Surveying the Agents of a Galaxy’s Evolution (SAGE) program for the Large (Meixner et al. 2006; Blum et al. 2006; Whitney et al. 2008; Bernard et al. 2008; Jones et al. 2015b) and Small (Gordon et al. 2011; Boyer et al. 2011; Sewilo et al. 2013) Magellanic Clouds (LMC/SMC), taken with the Spitzer Space Telescope (Spitzer). In addition to providing censuses of evolved stars, dust-production and mass-injection rates into the ISM were quantified (e.g., Matsuura et al. 2009; Boyer et al. 2012; Riebel et al. 2012; Srinivasan et al. 2016), with significant dust production ($10^{-4} M_\odot \text{ yr}^{-1}$) via oxygen-rich AGB stars found in the LMC ($\approx \frac{1}{2} Z_\odot$). The DUST in Nearby Galaxies with Spitzer survey (DUSTiNGS; Boyer et al. 2015a, 2015b; McQuinn et al. 2017; Boyer et al. 2017;

Goldman et al. 2019a) sampled 50 additional nearby (within 1.5 Mpc) galaxies using Spitzer 3.6 and 4.5 μm observations, finding that AGB stars are a major contributor of interstellar dust even at low metallicities. Recent works observing the nearby SF galaxy NGC 6822 (Lenić et al. 2024; Nally et al. 2024) with the JWST (Gardner et al. 2023) showcase its unparalleled IR sensitivity, improving upon earlier studies utilizing Spitzer and ground-based data (Jones et al. 2019; Hirschauer et al. 2020). Even with the crowded fields and large distance to IZw 18, JWST is capable of detecting and resolving individual evolved red stars, including RSGs and both oxygen- and carbon-rich AGB stars, as well as those undergoing substantial dust loss via superwind in which the most significant amounts of dust are produced (i.e., “x-AGB” stars; Blum et al. 2006; Boyer et al. 2011, 2015a).

JWST additionally offers incomparable sensitivity to dust-enshrouded young stellar objects (YSOs) and pre-main-sequence stars (e.g., Jones et al. 2023). The XMP abundance level, high SFR, and striking blue appearance of IZw 18 affirms the extreme nature of its SF regions. As YSOs are born in regions of active star formation, they exhibit strong IR excess as their light is absorbed and reemitted by their surrounding cool dusty envelopes and accretion disks. Previous photometric studies with earlier facilities were only capable of detecting the most massive such stars ($\gtrsim 8 M_{\odot}$), which account for only roughly one in every 10,000, and star clusters (Whitney et al. 2008; Gruendl & Chu 2009; Carlson et al. 2012; Nayak et al. 2023). Because YSOs rapidly progress through the different stages of their evolution, observations are relatively rare. Detailed study of the population of young stars in IZw 18 will allow for a more complete understanding of the physical mechanisms which govern star formation in environments typical of the very early Universe.

For the first time, we present high-quality near- and mid-IR imaging of the BCD galaxy IZw 18 taken with JWST, which with its XMP level of chemical enrichment and high SFR represents an excellent accessible analog for high-redshift SF systems. In Section 2, we describe the observing strategy employed for this Guaranteed Time Observational program (PID: 1233; PI: M. Meixner), while in Section 3 we describe the data processing and analysis. Section 4 presents our initial results, including the first images of IZw 18 obtained using JWST as well as characterizations of various stellar source type candidates. We summarize the program in Section 5.

2. Observing Program

We imaged IZw 18 with JWST utilizing both the Near Infrared Camera (NIRCam; Rieke et al. 2005, 2023) and the Mid-Infrared Instrument (MIRI; Rieke et al. 2015; Wright et al. 2023) imager (Bouchet et al. 2015; Dicken et al. 2024). In total, 6.49 hr of integration time were split between NIRCam (~ 1.91 hr) and MIRI (~ 4.58 hr), across eight filters (four filters each) employed for the prime observations. The observations with NIRCam were taken on 2022 October 27, utilizing the F115W and F200W short-wavelength (SW) filters, alongside the F356W and F444W long-wavelength (LW) filters, with IZw 18 centered in the upper-left quadrant of Module B (B3), and Module A observing empty sky to provide suitable data for background contamination subtraction. Employing both the A and B modules with a single pointing, these observations covered a total field of view (FOV) of 9.7 arcmin^2 , with two $2\frac{1}{2} \times 2\frac{1}{2}$ fields separated by a $\sim 44''$ gap.

Observations with MIRI were taken with a single pointing on the same date, covering a FOV of $74'' \times 113''$. These utilized the F770W, F1000W, F1500W, and F1800W filters, centered on the galaxy. In addition, MIRI coordinated parallel observations were obtained of an off-target region of empty space with the F1000W and F1500W filters, also in a single pointing $74'' \times 113''$ in size.

The spatial coverage for the two instruments is illustrated in Figure 1, and the principal characteristics of this program are summarized in Table 2. At a distance of 18.2 Mpc (Aloisi et al. 2007), the angular resolution is $0''.04\text{--}0''.14$ ($\sim 3.5\text{--}12.4$ pc) in the NIRCam filters and $0''.3\text{--}0''.6$ ($\sim 26.5\text{--}53.1$ pc) in the MIRI filters, respectively. This provides an improvement over existing IR imaging with Spitzer (spatial resolution $\sim 2''$) by greater than an order of magnitude, and is of similar quality to optical-band imaging with HST.

2.1. NIRCam Strategy

Our NIRCam observations were taken with the FULL frame and without need for a primary dither pattern, as there were no mosaic gaps that needed to be filled in. The SHALLOW4 read-out pattern was selected in effort to optimize the signal-to-noise ratio (S/N), with one integration per exposure and six groups per integration. In addition, we implemented a four-point subpixel dither pattern to sample the point-spread function (PSF), which resulted in an overall exposure time of 1245.5 s for each of the SW+LW filter combinations (i.e., F115W + F356W and F200W + F444W).

Our selection of NIRCam filters was based on prior work on stellar populations at these wavelengths. The F115W and F200W filters are similar to standard Johnson J and K_s , respectively, while the F356W and F444W filters are similar to Spitzer IRAC [3.6] and [4.5], respectively. This allows for comparative studies with previous observations made of other galaxies, including the SAGE studies of the Magellanic Clouds (e.g., Blum et al. 2006; Meixner et al. 2006; Whitney et al. 2008; Gordon et al. 2011; Boyer et al. 2011), the DUSTINGS project, which observed many nearby SF galaxies (e.g., Boyer et al. 2015a, 2015b; McQuinn et al. 2017; Goldman et al. 2019a), and others (e.g., Nikolaev & Weinberg 2000; Jones et al. 2015a, 2018, 2019; Goldman et al. 2019b; Hirschauer et al. 2020).

Centering the spatial extent of IZw 18 within the upper-left quadrant of Module B (B3) was accomplished by requesting a special requirement which offset the position of the target by $55''.0$ in the “X” direction and $35''.0$ in the “Y” direction, centered at R.A. = 09:34:02.10, decl. = +55:14:25.00. This allows for uninterrupted spatial coverage of IZw 18 in the NIRCam SW FOV without relying on a restriction in spacecraft position angle.

2.2. MIRI Strategy

Observations with MIRI employed a four-point CYCLING dither pattern and a SMALL pattern size, utilizing the FULL subarray and FASTR1 read-out pattern, centered at R.A. = 09:34:02.00, decl. = +55:14:28.00. For the F770W and 1000W filters, we implemented strategies of 100 and 200 groups per integration, respectively, with one integration per exposure, for four total integrations each. The total exposure time for the F770W filter was 1110.0 s, while for F1000W it was 2220.0 s. With the next-longest-wavelength filter, F1500W used 110 groups per integration and two integrations per

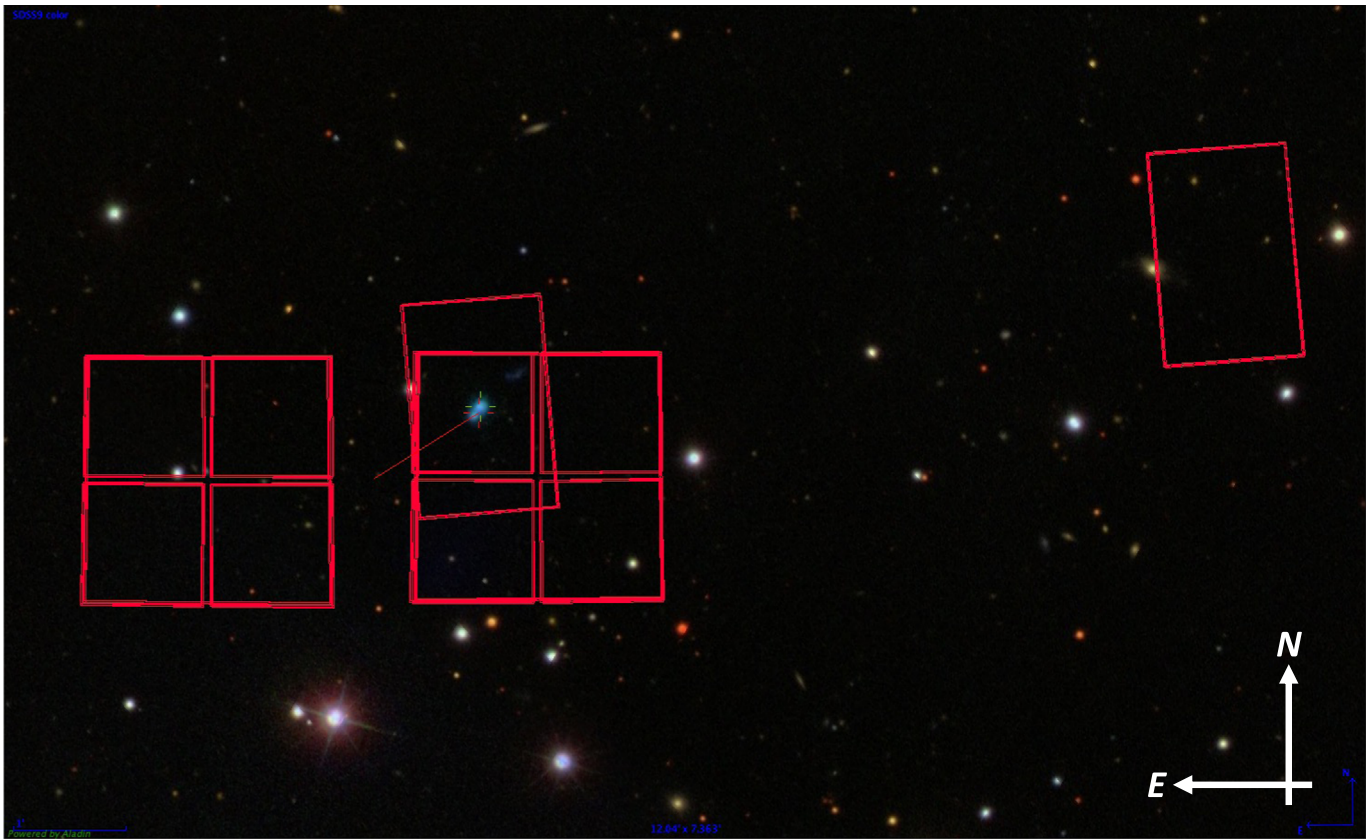


Figure 1. Imaging footprints for I Zw 18 with both NIRC2 (squares) and MIRI (rectangles) overlaid upon an optical-band image adopted from the Sloan Digital Sky Survey (York et al. 2000; Abazajian et al. 2004). North is up, while east is to the left. The compact extent of the galaxy, seen as the small, blue, double-lobed object, allows for only a single pointing with each instrument. A small position offset (+55''0 in x ; +35''0 in y) from center (between the two NIRC2 modules) ensured I Zw 18's placement within the upper-left quadrant of NIRC2 Module B (B3), regardless of the spacecraft's position angle. While NIRC2 Module A (middle left) provides a suitable region of blank space for performing background correction, for MIRI a coordinated parallel observation was included (upper right).

exposure, resulting in eight total integrations totaling 2453.1 s. The longest-wavelength MIRI filter, F1800W, necessitated selecting 88 groups per integration to avoid saturation of the sky background, achieving a long total exposure time of 5916.4 s by increasing the number of integrations per exposure to six, for 24 total integrations.

Our selection of MIRI filters was guided by the predicted JWST fluxes and color separations for IR-bright populations from Jones et al. (2017). Color-magnitude diagrams (CMDs) utilizing these long wavelengths are sensitive to the reddest and dustiest sources, offering unambiguous identification of evolved (RSGs and AGB stars) and young (YSOs) stellar populations via long-wavelength baselines. The longer-wavelength MIRI filters F2100W and F2550W were *not* chosen despite the wider possible baselines of its CMDs, owing to a steep drop-off in sensitivity which would have required substantially longer integration times to achieve comparable S/N. Separation of source types was determined to be equivalently achievable using the F1800W filter with shorter exposure times. Finally, detection of polycyclic aromatic hydrocarbon emission is accomplished with the F770W filter, and the F1000W filter is sensitive to the 10 μm silicate feature.

In addition, a MIRI coordinated parallel observation (when NIRC2 was prime) was included to provide background comparison images useful for contaminant source subtraction. The MIRI coordinated parallel image was obtained in the F1000W and F1500W filters utilizing a FULL subarray, and designed to maximize available integration time as determined

by the NIRC2 prime observations. We utilized a FASTR1 read-out pattern, with 112 groups per integration and one integration per exposure over the four total dithers, resulting in a total exposure time of 1243.2 s per filter. Data acquired from the MIRI parallel field are not considered further in this paper.

3. Data Reduction and Source Extraction

3.1. Data-reduction Methodology

Processing of the NIRC2 imaging data was carried out utilizing a slightly modified version of the JWST official pipeline (version 1.7.2) through all three stages. These modifications corrected for $1/f$ noise and flat-field correction noise, World Coordinate System alignment issues, and included the most recent NIRC2 calibration files at the time of data processing. For Stage-1 data, we used `jwst_1069.pmap` of the Operational Pipeline Calibration Reference Data System (CRDS), produced on 2022 October 3 with on-sky derived photometric zero-points (Boyer et al. 2022; Gordon et al. 2022). A frame0 correction was implemented to recover stars saturated in the first group (~ 21 s), but were unsaturated in the first 10.7 s comprising frame0 (`ramp_fit.suppress_one_group=False`). For Stage-2 output files (`*_cal.fits`), `imageroverf.py` was used to correct for $1/f$ noise.¹⁴ Because the small FOV contained few suitable Gaia reference stars, astrometric alignment was done relatively between frames and filters. A simple source catalog was created

¹⁴ <https://github.com/chriswillott/jwst>

Table 2
Observing Parameters for NIRCам and MIRI Imaging

Filter	Field	Read-out Pattern	Groups/Int.	Int./Exp.	Dithers	Total Exp. Time (s)
F115W	NIRCам Prime	SHALLOW4	6	1	4	1245.465
F200W	NIRCам Prime	SHALLOW4	6	1	4	1245.465
F356W	NIRCам Prime	SHALLOW4	6	1	4	1245.465
F444W	NIRCам Prime	SHALLOW4	6	1	4	1245.465
F770W	MIRI Prime	FASTR1	100	1	4	1110.016
F1000W	MIRI Prime	FASTR1	200	1	4	2220.032
F1500W	MIRI Prime	FASTR1	110	2	4	2453.135
F1800W	MIRI Prime	FASTR1	88	6	4	5916.385
F1000W	MIRI Parallel	FASTR1	112	1	4	1243.218
F1500W	MIRI Parallel	FASTR1	112	1	4	1243.218

Note. Observations for JWST PID: 1233 executed on 2022 October 27.

from a single arbitrary exposure in the F115W filter using source detection from the JWST pipeline. Alignment of the remaining F115W frames and frames from the remaining filters to this source catalog was accomplished using the JWST/Hubble Alignment Tool (JHAT).¹⁵ Because alignment to Gaia was already accomplished via JHAT, the Stage-3 `tweakreg` step was skipped.

JWST pipeline version 1.12.0 with CRDS version 11.17.9 and context `jwst_1149.pmap` were used in the creation of the final F770W imaging data. The remaining MIRI filters were subsequently processed using CRDS version 11.17.6 and context `jwst_1179.pmap`. The new CRDS context included updates for the MIRI Medium Resolution Spectrometer and thus does not affect the MIRI imaging data we present here. Flux-calibrated images in all four filters were produced by processing the raw MIRI ramp files using `Detectort1Pi` pipeline, with the output being run through `Image2Pipeline` with default parameters. Before combining the individual dithers into a final image, we aligned the F770W `Image2Pipeline` files (`*_cal.fits`) to the NIRCам F444W point-source catalog. We then applied the same astrometric corrections to the remaining MIRI filters. Following image alignment, we perform instrumental background subtraction following the method outlined in Nally et al. (2024). For each filter, we first median combine all dithers. Because IZw 18 is present in each of these exposures, however, the median-combined backgrounds are not free of structure. We therefore select unaffected detector rows and columns and map these to the detector plane to produce a model background, which we then subtract from each individual exposure (see Nally et al. 2024; Dicken et al. 2024). Finally, the background-subtracted and F444W-aligned individual dither exposures were combined into final images using `Image3Pipeline` with the `tweakreg` step turned off.

3.2. Point-source Extraction

The extraction of point sources in IZw 18 was accomplished through use of the STARBUGII (Nally 2023) photometric tool and pipeline. This software is optimized for JWST observations of crowded stellar fields within complex environments, performing point-source extraction and band merging across multiple observations and wavelengths, utilizing core functions

Table 3
STARBUGII Parameters Used for All Photometry

Parameter	F115W	F200W	F356W	F444W	F770W
SIGSRC	5.4	5.5	4.8	4.8	6.5
SIGSKY	2	2.1	2	1.95	2.5
RICKER_R	1	1	1	1	1
SHARP_LO	0.4	-0.2	0	0	0
SHARP_HI	1.03	1.7	1.1	1.15	0.9
ROUND_LO/HI	± 2	± 2	± 2	± 2	± 2
APPHOT_R	1.5	1.5	1.5	1.5	2
SKY_RIN	3	3	3	3	4
SKY_ROUT	4.5	4.5	4.5	4.5	6
BOX_SIZE	2	2	2	2	5
CRIT_SEP	6	6	8	8	8
MATCH_THRESH	0.06	0.06	0.1	0.1	0.1
NEXP_THRESH	2	2	2	2	2

from the python PHOTUTILS (Bradley et al. 2022) package. Examples of programs which have employed STARBUGII for photometric study include Jones et al. (2023), Nally et al. (2024), Lenkić et al. (2024), and Habel et al. (2024). The complete set of the relevant STARBUGII parameters and their adopted values used for this program’s photometric extractions are listed in Table 3.

For each filter in NIRCам, we perform source detection using `starbug2 --detect` on the Stage-3 drizzled image. We locate sources that are $\sim 5\sigma$ above the sky level, and their location is measured by fitting centroids. Values of the *sharpness* and *roundness* are assigned en route to calculating a geometry for each point source. By setting an upper limit on *sharpness*, the measured ratio of source peak height to its median pixel value, remaining image artifacts are removed from the catalog, while setting a lower limit assists in removing faint peaks in the dust structure. Source symmetry is measured by the *roundness* parameter. Most resolved background galaxies, as well as further spurious detections within the dust structure, are removed by limiting the allowed level of asymmetry in the source profiles. The same routine was used to detect sources in the F770W MIRI image with modified detection parameters. Because the decrease in image resolution inhibited the detection of robust point-like sources in the longer-wavelength filters (F1000W, F1500W, and F1800W),

¹⁵ <https://github.com/arminrest/jhat>

bright sources in close proximity to other similar objects were instead merged into bright clustered regions that were not analyzed in this study.

Aperture photometry was performed for all four NIRCam filters (F115W, F200W, F356W, and F444W), plus the shortest-wavelength MIRI filter (F770W). For all NIRCam sources, we use a fixed radius of 1.5 pixels as well as a sky annulus of 3.0 and 4.5 pixels for the inner and outer radii, respectively. Aperture correction is interpolated between values given in CRDS `jwst_nircam_apcorr_0004.fits`. For the MIRI F770W band, the procedure is the same, however the aperture radius is increased to 2 pixels to account for the larger PSFs intrinsic to longer wavelengths, backgrounds are calculated within annuli of 4 and 6 pixels for the inner and outer radii, respectively, and `jwst_miri_apcorr_0005.fits` is used to calculate aperture corrections. Through inspection of the data quality array within the aperture of each source, we flag those with saturated, DO_NOT_USE, or SRC_JMP pixels (indicating a jump during detection) with the SRC_BAD flag in STARBUGII.

We only consider MIRI aperture photometry in the current work as the cruciform structure, which was known to contain up to $\sim 26\%$ of the flux in the F770W band (Gáspár et al. 2021), was not included in MIRI PSFs simulated by WEBBPSF at the time of the data reduction.

We perform PSF photometry on the stellar sources of I Zw 18 on the individual Stage-2 exposures of all four NIRCam filters. First, the nebulous emission which underlies our imaging data is modeled with the routine `starbug2 --background`. This places masking apertures of variable size, and fills them with the median pixel value within a local annulus. Values of the diffuse emission background are then measured for every pixel in the image by averaging all local pixels within a set box size, creating an effective representation of the nebulous emission. A clean image of the field, with nebulous emission estimate subtracted, is therefore created which enables accurate fitting of PSFs.

The tool WEBBPSF (Perrin et al. 2014) version 1.1.1 was then employed to generate a 5 arcsec PSF for each NIRCam detector subarray. After estimating and subtracting the nebulous background from each single exposure, PSF photometry was performed by running `starbug2 --psf` on the background-subtracted image, at locations defining source positions determined via the source detection. By leaving the centroid position as a free parameter, both the flux and position of each source are allowed to be fit. If the position of the new centroid differs from the initial guess determined during the source-detection step by more than $0''.1$, the flux is refit with the source’s position held fixed to the initial guess and is flagged with SRC_FIX, denoting the fit as being of poorer quality.

The calculation and application of instrumental zero-point magnitudes are necessary to calibrate the PSF photometry, as they are not normalized to physical units. A median difference in source magnitudes measured by the aperture photometry and PSF fitting is calculated using `starbug2 --calc-instr-zp`, allowing for the determination of instrumental zero-point magnitudes, which are then employed to calibrate the PSF photometry from STARBUGII to the AB magnitude system. These magnitudes are then converted to the Vega system using the reference file `jwst_nircam_abvegaoffset_0002.asdf`.

3.3. Stellar Source Catalog

Point-source catalogs for each of the four NIRCam filters were created via the methods described in Section 3.2. A band-matched catalog of point sources is then constructed for I Zw 18 by merging these catalogs produced for the individual filters using `starbug2-match --band`. The possibility of mismatching high-quality stellar data with any spurious detector artifacts is mitigated by excluding all sources in the individual filter catalogs with an error on their magnitude greater than 10%. While this may limit the potential for completeness of the master catalog, this strategy allows for better reliability overall.

First, we consider the catalog made from the shortest-wavelength filter data, for which the smaller PSF FWHM possesses astrometry of the highest certainty. These sources are then matched using a nearest-neighbor algorithm to sources in the next-shortest-wavelength catalog. The threshold for separation between filter catalogs increases with increasing wavelength (equivalently, as the size of the PSF increases), as adopting a single separation threshold which is larger than the astrometric uncertainty of, for example, the longest-wavelength NIRCam filter would result in mismatches with, for example, the shortest-wavelength NIRCam filter. For NIRCam, the SW filters (F115W and F200W) are matched using a threshold of $0''.06$, while the LW filters (F356W and F444W) are matched and added using a threshold of $0''.10$. Any unmatched sources outside of the separation threshold are then appended to the end of the catalog, before the process is repeated with the next-shortest-wavelength filter data which remains. We note that, for the nearest-neighbor search method, the position coordinates for the source are adopted from the shortest-wavelength catalog from which said source initially appears. This allows us to retain the greatest possible positional accuracy for each source.

Due to I Zw 18’s relatively high position with respect to the Galactic plane, along with the galaxies’ compact size and small FOV of our observations, the number of contaminating stars inhabiting the foreground is negligible.

To avoid artifacts at the edges of the detectors and unresolved background galaxies impacting our photometric analysis, an elliptical region approximately $55'' \times 40''$ aligned along I Zw 18’s semimajor axis was defined. Only point sources detected within this region were considered to be members of I Zw 18 in our analysis. In addition, point sources from Component C were extracted from within a $30'' \times 22''$ elliptical region centered on this system, while carefully avoiding the detector edge. The proximity of Component C to the detector edge makes robust separation between real sources and artifacts challenging; here, we present preliminary results in Section 4.3, with a more detailed analysis to follow as the JWST calibrations improve.

4. Results and Discussion

4.1. Images

Our NIRCam-only image (Figure 2) reveals an extreme population of bright, blue, recently formed massive stars, with positions centered upon two primary lobes of star formation, consistent with earlier optical/near-IR studies of I Zw 18 utilizing HST (e.g., Hunter & Thronson 1995; Östlin 2000; Cannon et al. 2002; Izotov & Thuan 2004). An assortment of vivid red stellar sources distributed about the galaxy accentuates the presence of luminous evolved stars. Also apparent are



Figure 2. Four-color near-IR composite image of I Zw 18 in NIRCcam F115W (dark blue), F200W (light blue), F356W (orange), and F444W (red). Image orientation is such that north is to the left, while east is down. An underlying red population of older stars is complemented by hot, massive stars, identifiable by bright, blue sources occupying the NW and SE components. These H II regions are swaddled among a cocoon of gas and dust, while resolved background galaxies populate the image outskirts. Stellar sources affiliated with Component C are visible at the top of the image, just left of center. The image resolution afforded by NIRCcam imaging is $0.''04\text{--}0.''14$, roughly equivalent to that of HST's optical bands. This image was made by ESA/NASA/CSA/STScI.

the large supershells of dust and ionized gas carved out by previous star formation and SNe activity. These align with extant maps of emission, including continuum-subtracted $H\alpha$ and $H\beta$ from Cannon et al. (2002), which found significant concentrations of dust along such structures. Resolved background galaxies are apparent throughout the image spanning a variety of orientations and morphology. Stellar sources associated with the companion system Component C are visible at the top of the image, just left of center. Gas structure of the ISM is noticeably absent by comparison, consistent with

a generally older population of stars bereft of recent star formation (see Section 4.3 for further analysis).

Images of I Zw 18 made utilizing MIRI filters (Figure 3) emphasize the ISM structure of the galaxy via diffuse emission, with loops and filaments tracing a complex gas morphology, and clumpy nature reflecting that of the neutral and molecular gas component (e.g., van Zee et al. 1998; Cannon et al. 2002, 2005). In addition, we see an amalgamation of light originating from the reddest stellar populations, including AGB stars and embedded YSOs, corresponding to the two major SF

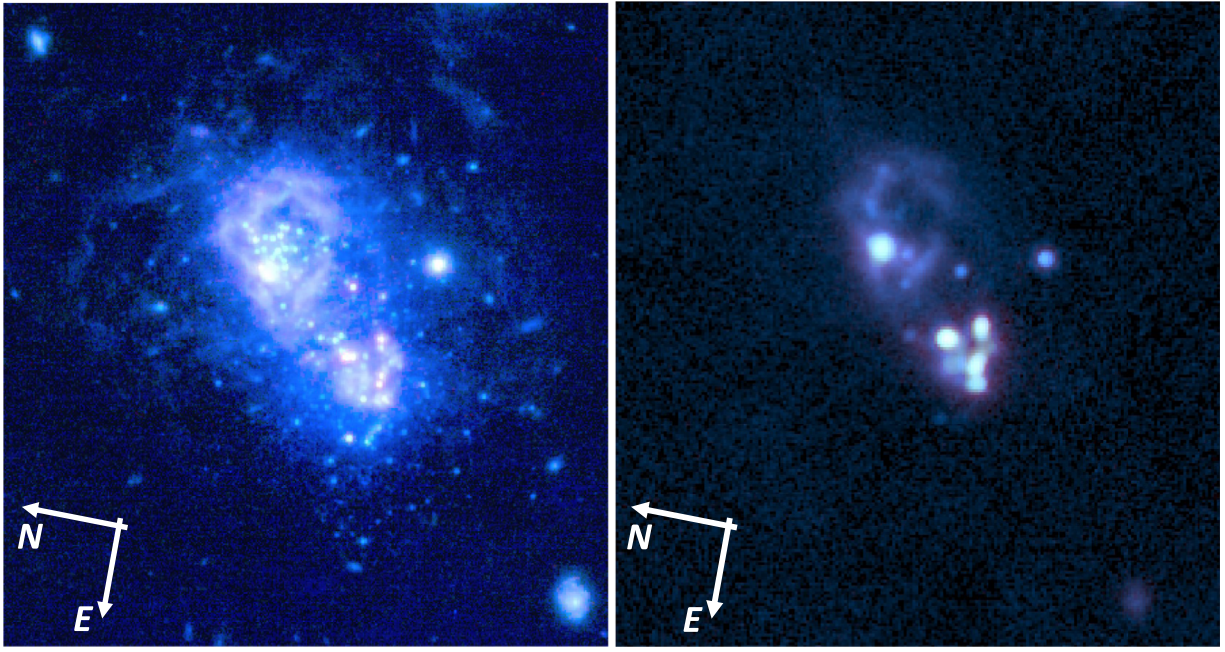


Figure 3. Three-color composite images of I Zw 18 in near- and mid-IR filters. A combination utilizing NIRCcam F356W, F444W, and MIRI F770W (left) emphasizes the ISM structure of the galaxy in relation to its recent star formation. The longer-wavelength MIRI F1000W, F1500W, and F1800W filters (right) showcase bulk emission properties of the major SF regions. Image orientations are such that north is to the left, while east is down, matching that of Figure 2. Located at a distance of 18.2 Mpc, these imaging data present resolutions of $0.''04$ – $0.''14$ in NIRCcam and $0.''3$ – $0.''6$ in MIRI.

lobes (the NW and SE components). These, together with a change in morphology and emission peak with increasing wavelength seen in Spitzer imaging data by Wu et al. (2007), are resolved here into individual stars, clusters, and ISM structure.

Single-filter false-color images for each of the four NIRCcam (Figure 4) and four MIRI (Figure 5) filters are presented which emphasize details observed in each band. The spatial distribution of all point sources extracted from both I Zw 18’s main body ($n = 1,520$; gray dots) and Component C ($n = 286$; red open circles) are shown in Figure 6.

4.2. Color–Magnitude Diagrams

We construct near-IR CMDs using NIRCcam data, which enabled our investigation of the various stellar populations inhabiting I Zw 18 (Figure 7). Our primary diagnostic CMD is F200W versus F115W–F200W, which possesses the highest sensitivity to faint sources and therefore offers the largest potential pool of candidate stars ($n = 689$). This combination of filters was employed as a JWST-specific facsimile for standard diagnostic plots, enabling comparison with previous dusty and evolved star studies utilizing Spitzer bands such as SAGE and DUSTiNGS (e.g., Blum et al. 2006; Boyer et al. 2011, 2015a, 2015b). In addition, the methods executed by this study mirror recent stellar populations imaging work undertaken with JWST of other extragalactic sources, including NGC 6822 (Nally et al. 2024; Lenkić et al. 2024) and NGC 346 (Jones et al. 2023; Habel et al. 2024).

The structure of points populating this CMD can be roughly described as two primarily vertical columns extending from a common foundation, which terminates as the detection threshold is reached at magnitudes fainter than $F200W \approx 28.0$. At this level, the sensitivity limitations of the photometry results in a broad scatter. Points which make up the blueward (left-side) column of sources represent young stars of the upper main

sequence (UMS), with those exhibiting the brightest magnitudes being the most massive. The redward column of sources is principally populated by evolved stars. Here, fainter sources are on the red giant branch (RGB), while at brighter luminosities these stars are chiefly He-core-burning RSGs and those on the AGB. Based on the distance modulus to I Zw 18, the tip of the red giant branch (TRGB) is estimated to be located at $F200W \approx 25.6$. A luminosity function for all galaxy stars (gray) and only those stellar sources populating the evolved star column of sources in this CMD (red) is presented as Figure 8. An apparent discontinuity of sources at $F200W \approx 25.6$ supports this estimation of the TRGB location, though a combination of large photometric uncertainties and small number statistics prevents definitive identification of the TRGB.

In order to assist our preliminary point-source type classifications, we have included for reference PARSEC isochrones of an XMP stellar population ($Z = 0.0003$; e.g., Bressan et al. 2012) at ages of 1, 10, 25, 50, 100, 250, 500 Myr, 1, 2, 5, and 10 Gyr, overlaid on this CMD (see Figure 9). The distribution of sources seen reflects the existence of both older and younger populations; for a thorough examination of the star formation history (SFH) of this galaxy as discerned by the photometric data obtained with NIRCcam, see Bortolini et al. (2024, submitted). The overall numbers for point-source identifications described in the following subsections from the young star and evolved star branches, including their respective dust-enshrouded candidates (Section 4.2.1), plus YSO and YSO cluster candidates (Section 4.2.2), are summarized in Table 4.

4.2.1. Dusty Evolved Star Candidates

Identification of dust-enshrouded stellar source candidates in I Zw 18 using IR photometry was accomplished by examining a CMD employing our most widely separated NIRCcam filter

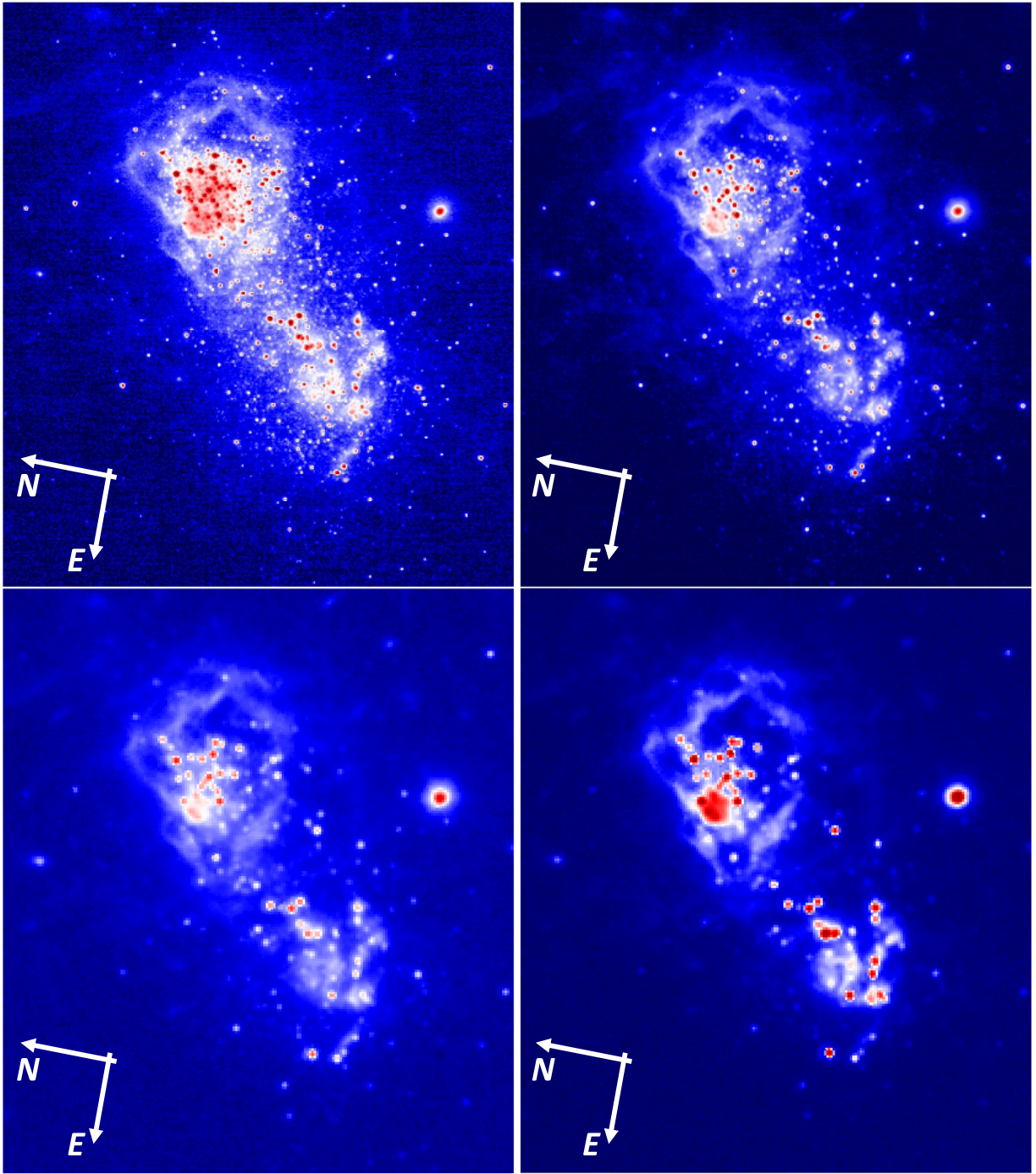


Figure 4. Single-filter false-color images for NIRCam F115W (upper left), F200W (upper right), F356W (lower left), and F444W (lower right). Clusters of sources emitting in the near-IR reside predominantly in the NW and SE lobes of active star formation. Detail of the stellar population is revealed from within the obscuring ISM, and IR-bright sources such as AGB stars, RSGs, and bright YSOs become progressively more conspicuous with increasing wavelength. Image orientations are such that north is to the left, while east is down.

data (F444W versus F115W–F444W; Figure 10). At these longer wavelengths, the numbers of detected point sources ($n = 183$) diminish in comparison to our primary diagnostic CMD. This large color baseline, however, affords a robust separation between dusty and nondusty stellar types: Any source detection with a color value $F115W - F444W > 0.0$ may be considered to be at least somewhat enshrouded in dust. In order to account for photometric uncertainties, multiple ages, variance in metallicities, and other broadening effects, we have

elected to implement a more conservative color cut at $F115W - F444W = 0.5$. Our dust-enshrouded source candidates therefore require detection in all three of the F115W, F200W, and F444W filters; a star becomes ineligible for inclusion in our high-confidence catalog if it is missing from any one filter’s detected source list. While the overall effect is that we are possibly missing some real dust-enshrouded source candidates in our study, we are opting to remain conservative. We also note that, while the MIRI F770W filter provides for a yet-

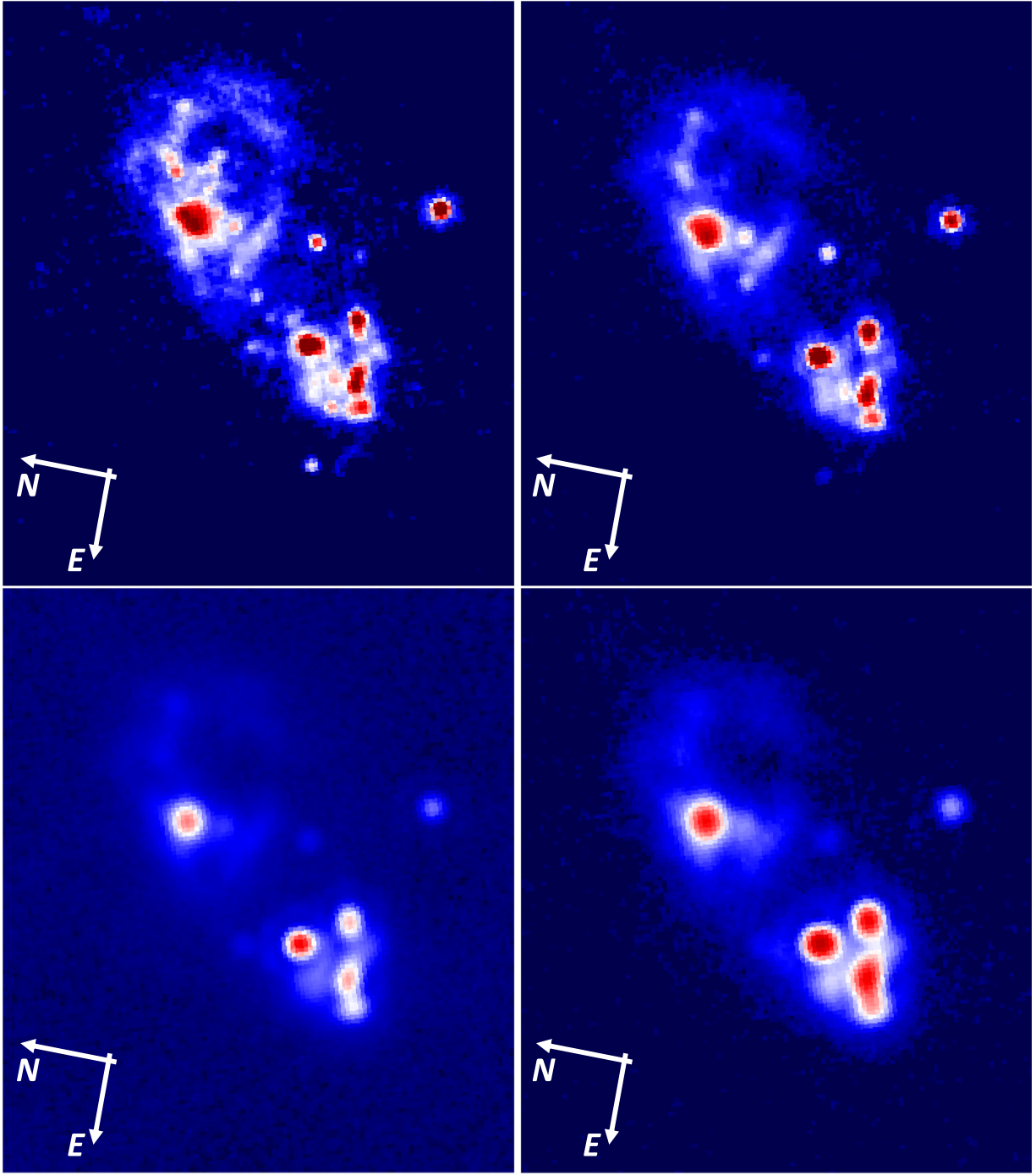


Figure 5. Single-filter false-color images for MIRI F770W (upper left), F1000W (upper right), F1500W (lower left), and F1800W (lower right). Strong mid-IR emission is correlated with the NW and SE lobes. Emission from amalgamated IR-bright stellar sources (such as YSO clusters inhabiting massive SF regions) becomes pronounced at longer wavelengths. Image orientations are such that north is to the left, while east is down.

longer color baseline, the paucity of sources detected via the F115W–F770W color for our data diminishes its utility as a diagnostic tool. At the distance to I Zw 18 (18.2 Mpc), the resolution and sensitivity of MIRI F770W are substantially less than that of NIRC2 F444W, such that including this baseline could result in blending in the F770W filter, leading to source mismatches between catalogs.

The F444W versus F115W–F444W CMD (Figure 10) employed to characterize dust-enshrouded source candidates in I Zw 18 bears resemblance to the $[4.5]$ versus $K-[4.5]$ CMD used by the Dell’Agli et al. (2019a) study of Sextans A, a

nearby ($D = \sim 1.32$ Mpc; Dolphin et al. 2003) low-metallicity ($12 + \log(\text{O}/\text{H}) \approx 7.6$; Skillman et al. 1989; Pilyugin 2001) SF dwarf galaxy (see their Figures 2 and 3). While Dell’Agli et al. (2019a) utilized this plot alongside evolutionary model tracks of metal-poor stars in order to make distinctions between evolved star populations (RSGs, O-rich AGBs, C-rich AGBs), we do not attempt to make equivalent early distinctions. Because of the larger distance to I Zw 18, our data suffers from higher photometric uncertainties as a consequence of crowding effects.

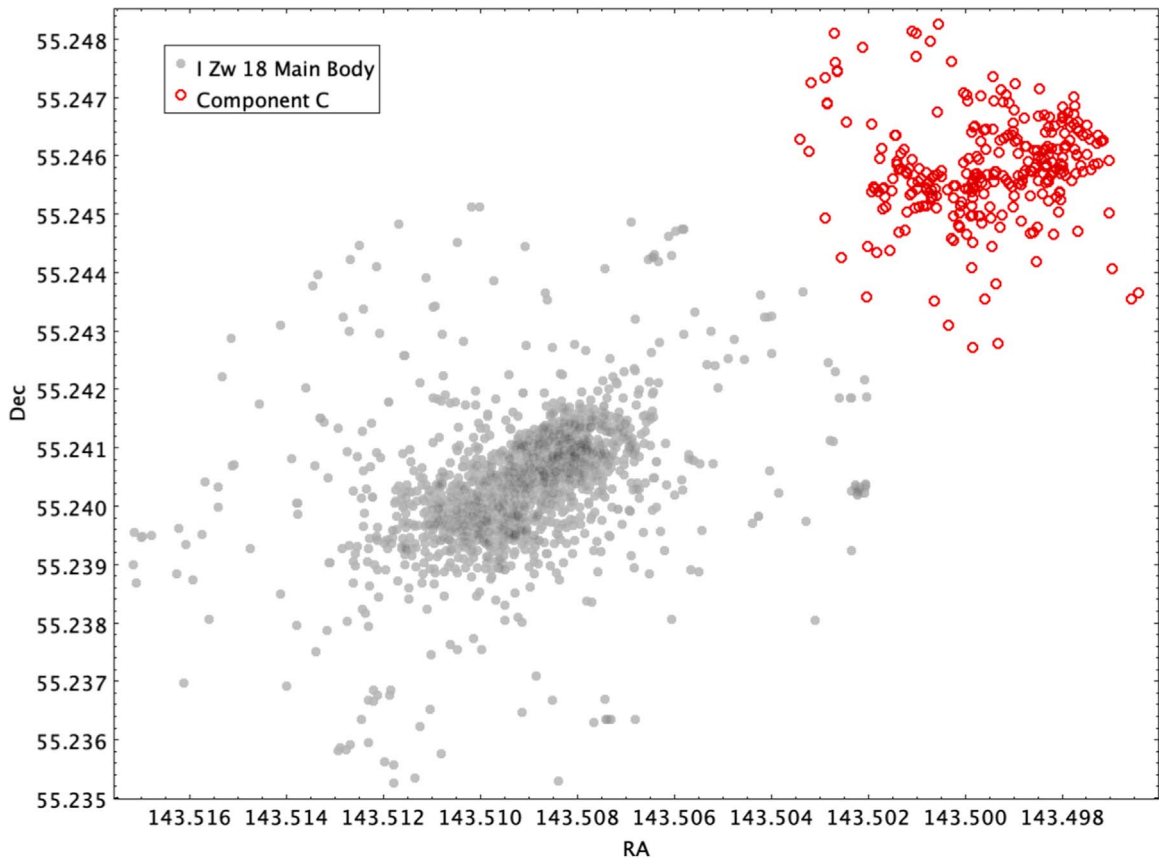


Figure 6. Spatial distribution of NIRCcam point sources affiliated with the main body of I Zw 18 ($n = 1520$; gray dots), identified using a $55'' \times 40''$ elliptical region centered on the galaxy’s main body. In addition, point sources affiliated with Component C ($n = 286$; red open circles) are extracted from a $30'' \times 22''$ region $\sim 36''$ away from the center of I Zw 18, which avoids artifacts from the detector edges.

For our list of dust-enshrouded source candidates identified from this CMD, we additionally required each detection to have been found in the F200W versus F115W–F200W CMD located above the TRGB (F200W = 25.6). We note that, while some additional bona fide dust-enshrouded source candidates are likely to lie below this TRGB, we have elected to exclude them here for the sake of remaining conservative with our estimates, and to reflect larger photometric uncertainties at these magnitudes. For objects inhabiting the right-side (evolved stars) branch of the F200W versus F115W–F200W CMD, those which are additionally identified as being dusty in the F444W versus F115W–F444W CMD are expected to be AGB stars, RSGs, and bright YSO clusters. The fewer dusty sources of the left-side (young stars) branch of the F200W versus F115W–F200W CMD are likely RSGs. In total, we find $n = 119$ dusty source candidates in the F444W versus F115W–F444W CMD, which are signified both in Figures 7 and 10 as overlaid green dots. Of these, $n = 99$ belong to the evolved stars branch, while $n = 20$ belong to the young stars branch. Overall, of the $n = 226$ sources populating the evolved stars branch, the $n = 99$ robust dust-enshrouded source candidates represent $\sim 43.8\%$ of the total. While the $n = 20$ dust-enshrouded source candidates on the young stars branch constitute only $\sim 17.2\%$ of the total ($n = 116$), these include the majority of bright sources expected to be RSGs.

Stars inhabiting the AGB represent the final evolutionary stage of low- to intermediate-mass ($\sim 0.6\text{--}10 M_{\odot}$) MS progenitors, and are believed to be a major contributor of interstellar dust. Of interest to this observing program in

particular are thermally pulsing (TP-AGB) stars, which lie above the TRGB. We may classify these AGB stars into two major categories: oxygen- and carbon-rich (O-rich and C-rich, respectively). MS progenitors with masses $\sim 3\text{--}8 M_{\odot}$ evolve to become AGB stars which are rich in oxygen, but have short lifespans ($t_{\text{life}} \sim 30\text{--}200$ Myr). While they are capable of producing dust relatively quickly after having formed, they are not expected to enrich the ISM with s -process elements in metal-poor environments to the same degree as AGB stars with lower initial masses ($\sim 1\text{--}3 M_{\odot}$), which are more prevalent (e.g., Lugaro et al. 2003; Karakas & Lugaro 2016; Karakas 2010). Fewer s -process elements may result in fewer nucleation sites for dust growth in the ISM. These stars possess longer lifespans ($t_{\text{life}} \sim 200$ Myr–3.6 Gyr; Karakas & Lattanzio 2003; Ventura et al. 2013; Boyer et al. 2015a), during which they experience repeated third dredge-up episodes (Kwok 2000) that lead to their becoming increasingly carbon-enriched (Karakas & Lattanzio 2014). O- and C-rich TP-AGB stars may therefore be distinguished from one another based on the dominant chemistries of their photospheres. If the value of the ratio of carbon to oxygen (C/O) is > 1 , the AGB star is C-rich, while a C/O value < 1 is O-rich. Dust species born from these populations depend upon the dominant element, such that carbonaceous dust grains are produced by C-rich AGB stars, while silicates are produced by O-rich AGB stars.

The stellar mass value at which the distinction between O- and C-rich AGB stars occurs exhibits a dependence on metal abundance, decreasing from $\sim 3 M_{\odot}$ as metallicity gets lower:

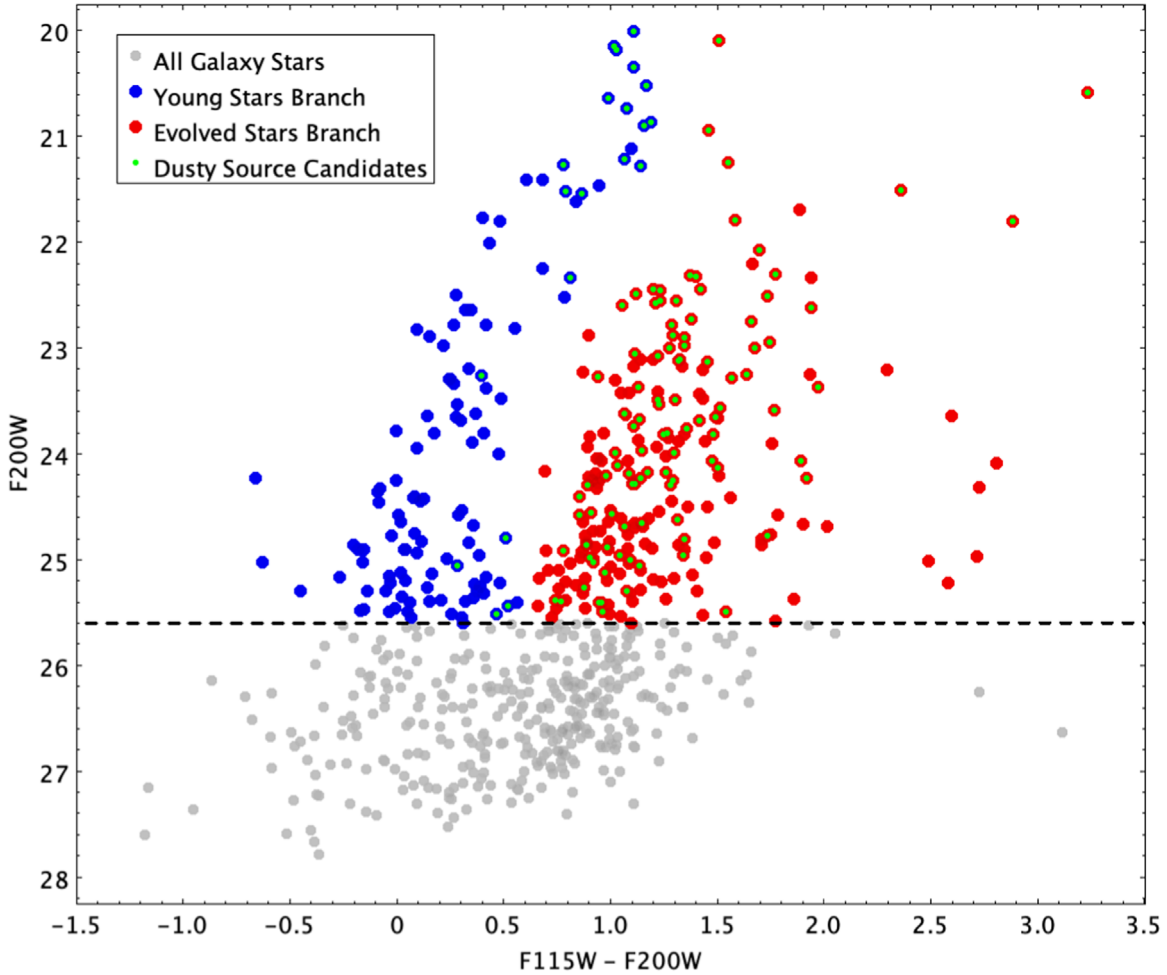


Figure 7. Primary diagnostic CMD for point sources extracted from an elliptical region encompassing the main body IZw 18. This utilizes the two SW NIRCcam filters (F200W vs. F115W–F200W) and offers the largest potential pool of candidate stars for this study ($n = 689$). Stellar source type candidates above the TRGB (F200W ≈ 25.6 ; dashed line) are illustrated as either left branch (blue) or right branch (red), representing young or evolved stars, respectively. Those colored circles overplotted with a green dot denote characterization as dust-enshrouded candidates (see Section 4.2.1). Dusty objects on the left branch of points are most likely RSGs, while those on the right branch of points are a mixture of AGB stars, RSGs, and bright YSOs.

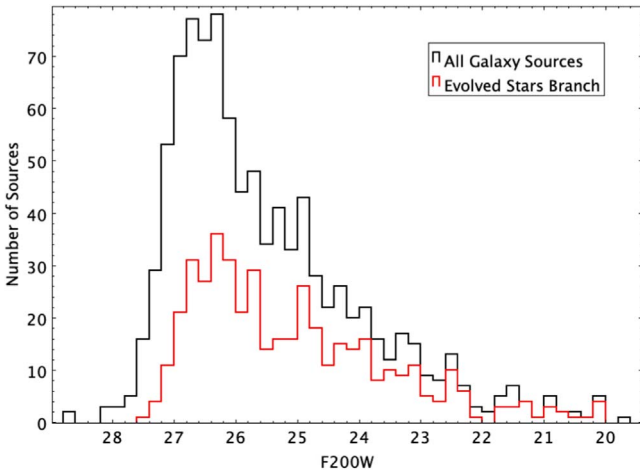


Figure 8. Luminosity function for all galaxy stars (gray) and stellar sources populating the evolved star spur only (red) in the F200W filter, which makes up the y-axis of our primary diagnostic CMD. A discontinuity of detections is apparent at F200W ≈ 25.6 , supporting the expected location of the TRGB.

The condition of $C/O > 1$ is reached more easily for stars in environments with lower abundances of oxygen. In the case of extremely low metallicities, such as that exhibited by IZw 18,

the threshold for producing more C-rich stars may occur as low as $\sim 2.5 M_{\odot}$ (Dell’Agli et al. 2018).

Without the wider color baselines afforded by MIRI photometry, robust segregation between O- and C-rich AGB stars is not possible. Many of the evolved star branch sources identified in the F200W versus F115W–F200W CMD (Figure 7; red points), however, are expected to be TP-AGB stars. In addition, considering the extremely low metallicity of IZw 18, many of these TP-AGB candidate stars are expected to be C-rich. The distribution of dust-enshrouded evolved stars (red points with overplotted green dots) permeates the parameter space occupied by the F200W versus F115W–F200W CMD’s evolved star branch, suggesting the presence of many dusty C-rich AGB star candidates in IZw 18.

The locations of the evolved star branch sources in this galaxy are illustrated in Figure 11 (top) as red points, with dusty source candidates signified with overplotted green dots. Many of these objects are anticipated to be TP-AGB stars (other possibilities include massive YSOs, however positive classification will require spectral energy distribution model fitting; see Section 4.2.2 for more details), with the dustiest among them appearing to cluster around the large SF region located in the lower left (the SE lobe). Furthermore, these AGB

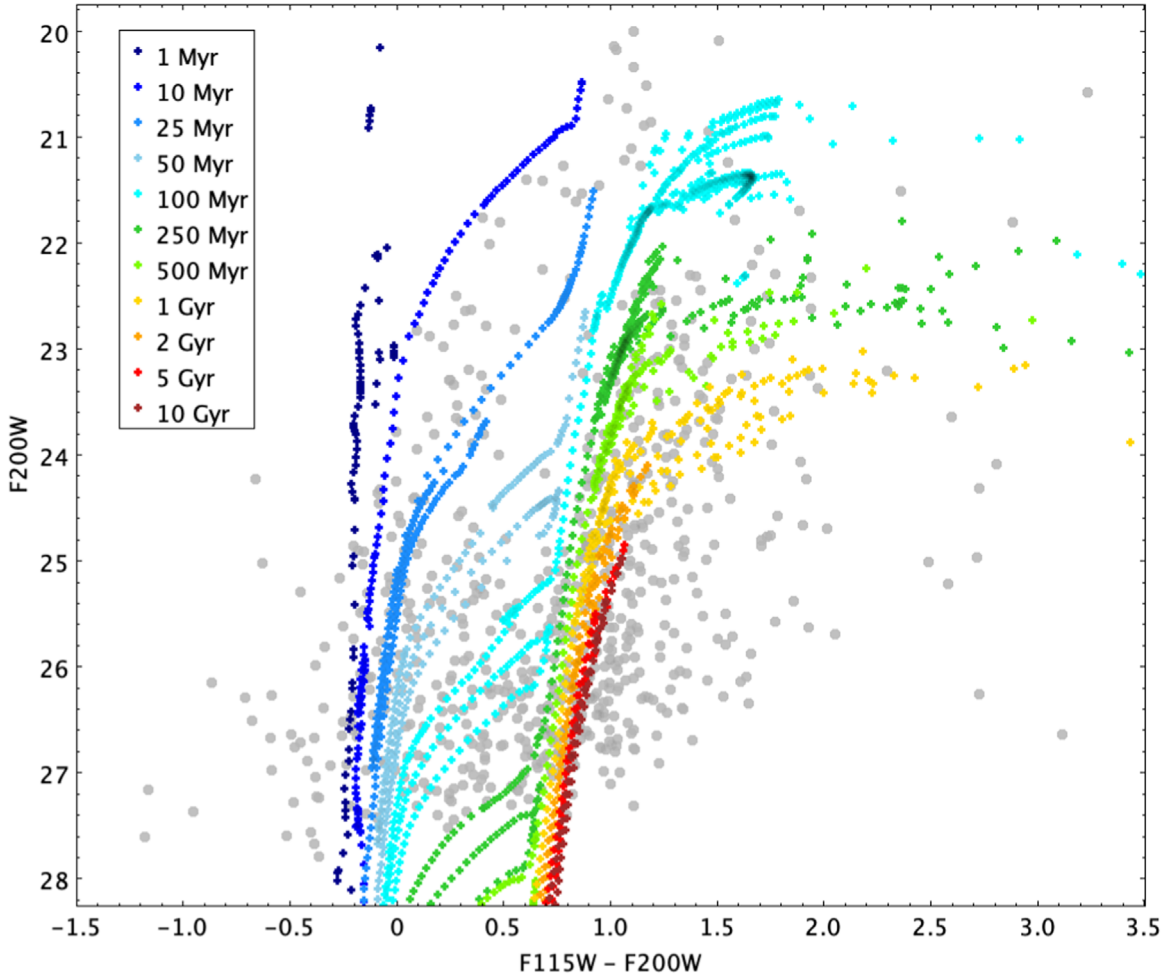


Figure 9. F200W vs. F115W-F200W CMD with overlaid PARSEC isochrones of an XMP stellar population ($Z = 0.0003$) at ages of 1, 10, 25, 50, 100, 250, 500 Myr, 1, 2, 5, and 10 Gyr.

Table 4
I Zw 18 Point-source Summary

Source Type	No. of Sources
Young stars branch	116
→ Dust-enshrouded	20
Evolved stars branch	226
→ Dust-enshrouded	99
YSO candidates	15

star candidates show consistency with identifications from past studies utilizing HST (e.g., Östlin & Mouhcine 2005).

Stars identified as RSGs are a late evolutionary phase of higher-mass ($\gtrsim 10 M_{\odot}$) MS progenitors which trace regions of recent star formation. These short-lived, cool, very luminous objects occupy color space coincident with TP-AGB stars, and are expected to be found alongside them in the F200W versus F115W-F200W CMD's evolved star branch. The majority of the brightest sources populating the left-side branch (Figure 7; blue points), however, are denoted as being candidate dust-enshrouded stars. These are therefore likely RSG candidates, as well, where they are illustrated in Figure 11 (bottom) as blue points with overplotted green dots. We find that these dusty left-branch RSG candidates are strongly clustered around the large SF region located in the upper right (the NW lobe),

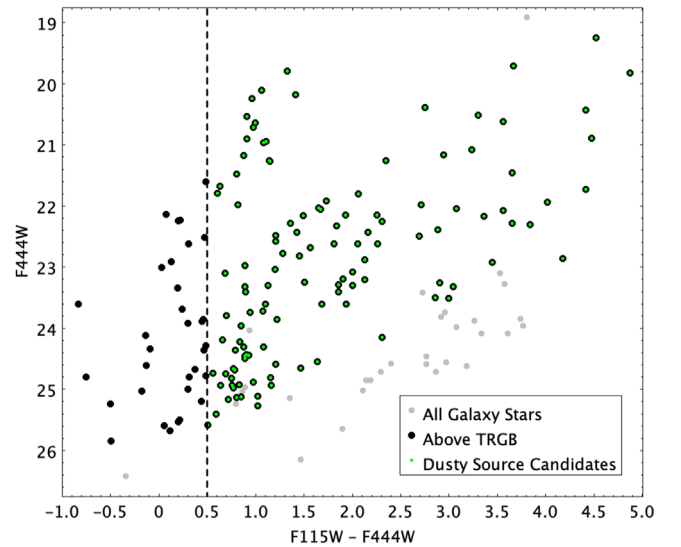


Figure 10. CMD constructed with our widest-possible color baseline (F444W vs. F115W-F444W) NIRC2 data, used to characterize dust-enshrouded object candidates. Sources which were found above the TRGB in our primary diagnostic CMD (F200W vs. F115W-F200W; see Figure 7) are denoted as black circles, while those below are shown in gray. Dusty source candidates in I Zw 18 are those found both above the TRGB and possessing a color value $F115W-F444W > 0.5$ (dashed line), and are presented here as black circles overplotted with green dots ($n = 119$).

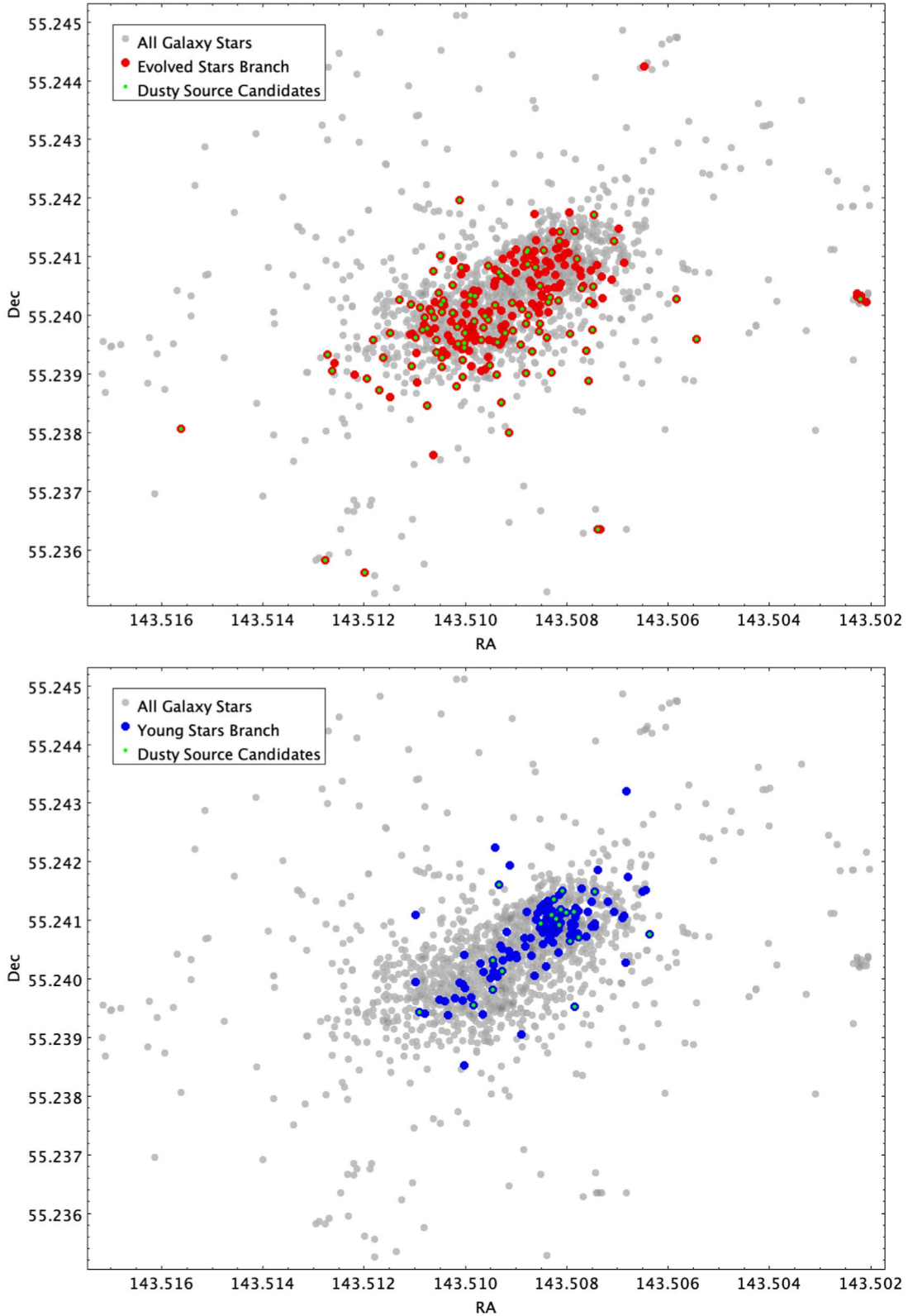


Figure 11. Spatial distribution plots for stellar sources populating the right branch ($n = 226$; top) and left branch ($n = 116$; bottom) of the F200W vs. F115W–F200W CMD, as found via photometric analyses of I Zw 18. Right-branch points indicated as red circles are a mix of evolved source candidates, including both O- and C-rich AGB stars as well as RSGs, in addition to bright YSOs. Left-branch points indicated as blue circles are predominantly hot young stars, including those populating the UMS, and bright RSGs. The dustiest of these objects, identified in the F444W vs. F115W–F444W CMD, are marked as overplotted green dots in both cases ($n = 99$ and $n = 20$, respectively). These sources are found chiefly clustered around the galaxy’s two major lobes of star formation (NW and SE).

opposite to that of the dusty TP-AGB stars discussed earlier. This broad demarcation of differently aged sources suggests that the bulk of the most recent star formation episode of the SE

lobe, populated predominantly with slower-evolving C-rich AGB stars, took place longer ago than that of the NW lobe, which is still inhabited by younger sources such as RSGs.

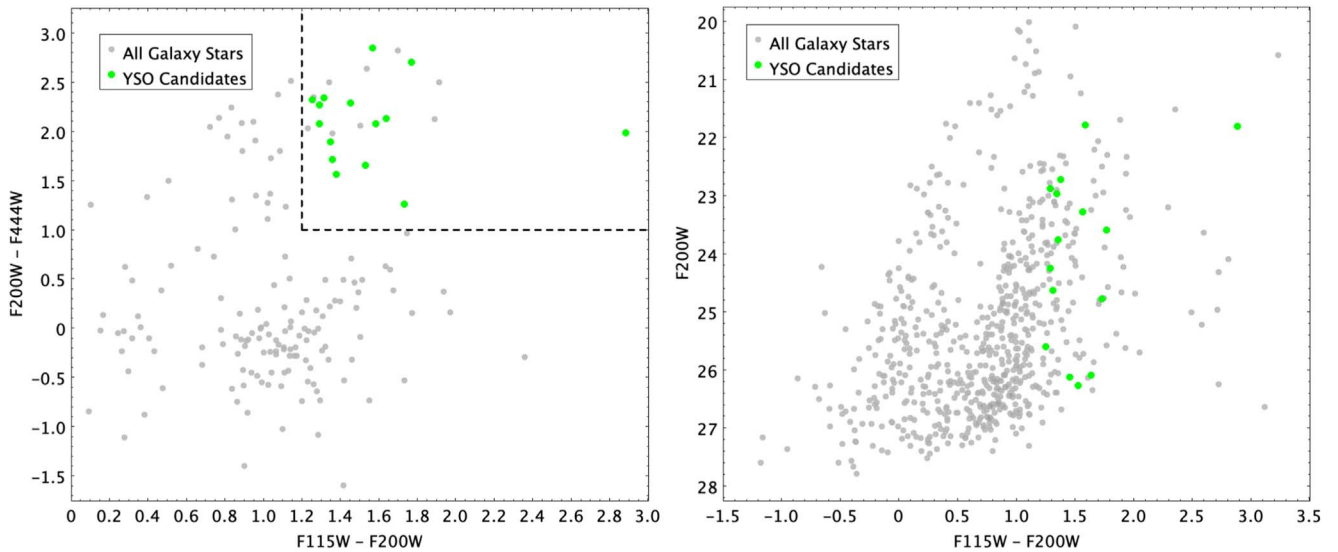


Figure 12. Unresolved YSO candidates ($n = 15$) identified in I Zw 18 presented as green circles. The F200W–F444W vs. F115W vs. F200W CCD (left) illustrates the color-selection criteria implemented by the JWST studies of Jones et al. (2023) and Habel et al. (2024) of the SF region NGC 346 in the SMC. These same sources are overlaid on the F200W vs. F115W–F200W primary diagnostic CMD, demonstrating positioning redward of the evolved stars branch, and to fainter magnitudes than the TRGB.

4.2.2. Young Stellar Object Candidates

The active star formation taking place in I Zw 18 makes it an excellent local analog for conditions which pervaded the early Universe, when heavy-element enrichment levels had yet to reach what is found today. YSOs are birthed in active star formation regions and exhibit strong IR excess as light is absorbed and reemitted by cool, dusty envelopes and accretion disks (Meixner et al. 2013; Seale et al. 2014). Identification of YSOs in I Zw 18 represents an improvement in our understanding of star formation mechanisms at the very low levels of chemical enrichment reminiscent of the early Universe, as resolved studies in higher-redshift galaxies that are comparably metal-poor are observationally precluded in all but a few rare circumstances. These YSOs trace regions of active star formation and emit even more strongly at long wavelengths than dusty AGB stars, particularly at the earliest stages of their lifetimes. This disk and its circumstellar envelope disperses as the protostar evolves (Robitaille et al. 2006), and so by consequence its dominant emission shifts from mid- to near-IR.

We identify YSO candidates in I Zw 18 as point sources exhibiting very red colors, similar to those of dust-enshrouded TP-AGB stars. This is accomplished by implementing the strategy featured in Jones et al. (2023) and Habel et al. (2024) for JWST study of YSOs in the SMC SF region NGC 346. The selection criteria require the source to be redward of the evolved stars branch from the F200W versus F115W–F200W CMD (with color $F115W - F200W > 1.2$). Additionally, the YSO candidates must satisfy the condition of $F200W - F444W > 1.0$, which was used for NGC 346 to establish the presence of IR excess. Finally, in order to correct for source contamination from background galaxies, which possess similar IR colors, we perform a final visual inspection of the YSO candidates in the NIRCcam F115W image to reject extended objects. We present these results in a color-color diagram (CCD) as Figure 12 (left), with $n = 15$ point sources plotted in green which inhabit the dashed line box illustrating these parameters. The location of these YSO candidates on the F200W versus F115W–F200W primary diagnostic CMD

(Figure 12, right) emphasizes the characteristic very red colors, as well as some magnitudes fainter than the TRGB ($F200W = 25.6$). We note that due to limitations of resolution and sensitivity at the distance to I Zw 18, any YSO candidates putatively identified in this study are likely to be unresolved clusters of several young stars.

The spatial distribution of YSO candidates in I Zw 18 is illustrated as Figure 13, shown again as green circles. Several sources appear to be grouped together within the SE lobe, consistent with a recent bout of star formation. YSO candidates are also situated along the outskirts of the NW lobe, where peak star formation activity is expected to have taken place longer ago. The locations of these sources appear to correlate with the strongest emission seen in MIRI F770W imaging (see Figure 5).

4.3. Component C

The companion system to I Zw 18, Component C, is offset from the main galaxy by $\sim 36''$. We present a comparison of the F200W versus F115W–F200W CMD with Component C point sources (open red circles) overlaid upon stars found in the main body (gray dots) as Figure 14.

Contrasting the distributions of sources, we see stellar populations which are roughly self-consistent between I Zw 18 and Component C ($n = 145$), forming distinctive left- and right-side branches that represent young and evolved stars, respectively. Of particular note is a comparative lack of Component C sources populating the bright end of the left-side branch, where the youngest UMS stars are expected to be located. This suggests that Component C is home to a generally older population of stars, where the youngest and hottest UMS sources have already transitioned to later evolutionary stages. An investigation of dusty targets, including selecting objects above the F200W versus F115W–F200W CMD TRGB ($F200W \approx 25.6$) and with $F115W - F444W$ color > 0.5 , yields a small number ($n = 26$) of sources denoted as filled red circles in Figure 14. These appear to predominantly inhabit the bright end of the F200W versus F115W–F200W CMD’s evolved

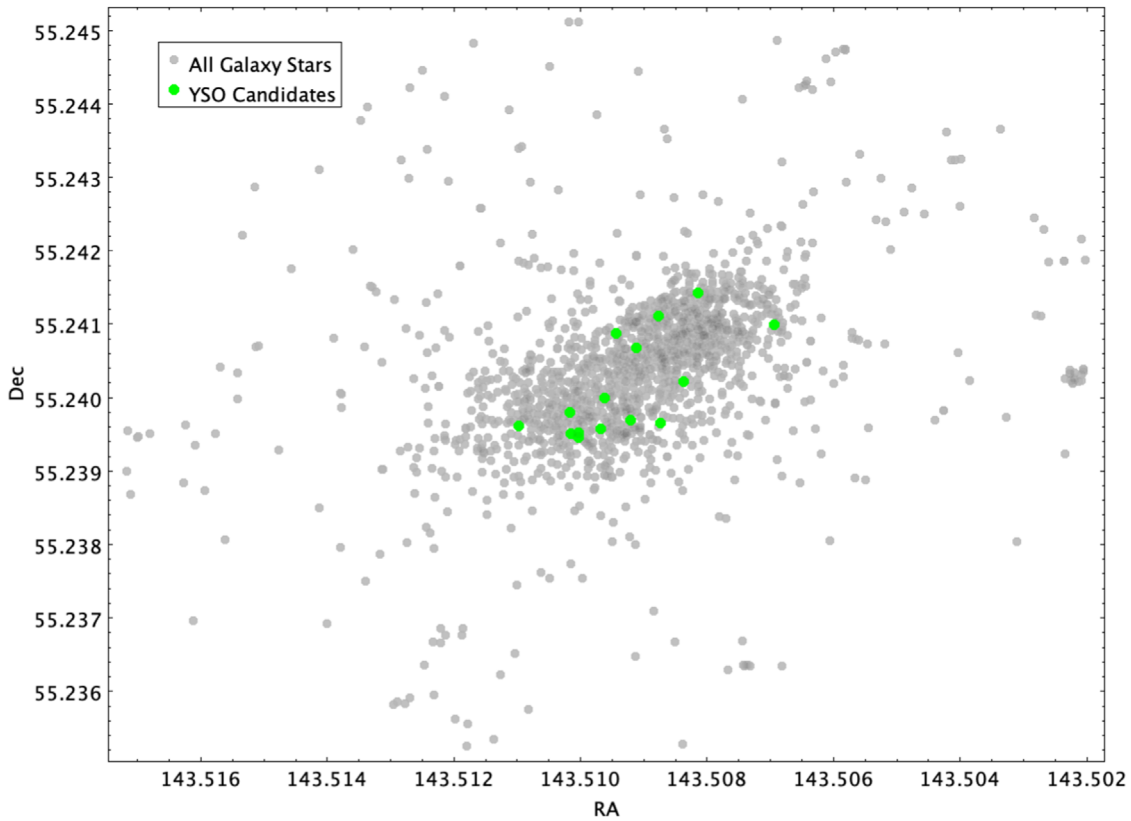


Figure 13. Spatial distribution plot for YSO candidates (green circles) in I Zw 18 identified via analysis of the F200W–F444W vs. F115W vs. F200W CCD. We find several sources grouped in the SE lobe of recent star formation, and along the outskirts of the older NW lobe.

stars branch. See Bortolini et al. (2024, submitted) for an exploration of the SFH for Component C.

5. Summary

We present for the first time JWST near- and mid-IR imaging data using NIRCam and MIRI of the XMP SF dwarf galaxy I Zw 18. The extremely low levels of heavy-element enrichment and high level of active star formation make it an excellent accessible analog for the types of small systems which are expected to have been ubiquitous in the very early Universe, and acted as major contributors to its overall chemical enrichment and reionization. With eight wide-band filters combining NIRCam (F115W, F200W, F356W, and F444W) and MIRI (F770W, F1000W, F1500W, and F1800W), we show deep, high-angular-resolution images at IR wavelengths comparable to that of optical-band HST data, and improved by over an order of magnitude over that of existing mid-IR Spitzer images. Our NIRCam data clearly show extreme populations of bright, recently formed massive stars, located predominantly among two central lobes of star formation (the NW and SE components). In addition, our MIRI imaging data demonstrate the bulk mid-IR emission characteristics of I Zw 18 at previously unattainable resolution, exhibiting a predominantly wispy and clumpy nature in the NW and SE components, respectively.

Utilizing the four NIRCam filters, we have constructed CMDs and performed color-cut analyses from which we identified candidate populations of dusty evolved stars (RSGs and AGB stars) in this galaxy, alongside bright YSOs. We employ a CMD utilizing the shortest-wavelength NIRCam filters (F200W versus F115W–F200W), which demonstrate the

greatest point-source sensitivity and therefore possess the largest number of sources, to analyze these populations. Having estimated the location of the TRGB, we divide those sources which lie above it ($F200W \approx 25.6$) into left- and right-branch populations, pertaining to younger (UMS) and older (evolved) stars, respectively. Harnessing next a CMD with wider color baseline (F444W versus F115W–F444W), we identify subsets of dust-enshrouded source candidates as those found above the TRGB and with color values >0.5 , many of which are expected to be C-rich TP-AGB stars, but which also include O-rich AGB stars, RSGs, and bright YSOs.

Further investigation of YSO or YSO cluster candidates was accomplished via the F200W–F444W versus F115W versus F200W CCD, building upon techniques implemented for recent JWST study of the NGC 346 SF region in the SMC. A small population of unresolved sources which satisfy the criteria $F115W-F200W > 1.2$ and $F200W-F444W > 1.0$ were isolated, with their locations in the galaxy correlated with MIRI F770W emission in the SE and NW lobes of star formation. Our findings suggest that the prevailing demographics of I Zw 18’s NW and SE star formation regions reflect that of younger and older stellar populations, respectively, consistent with a staggered SFH.

Point sources affiliated with I Zw 18’s companion system, Component C, were also extracted. A similar analysis was performed, finding CMD structures closely matching those constructed from the galaxy’s main body. We find a comparative lack of detections in the CMD location representative of Component C’s young, hot star population, suggesting that the bulk of its most recent star formation episode took place longer ago than that of I Zw 18’s main body, consistent

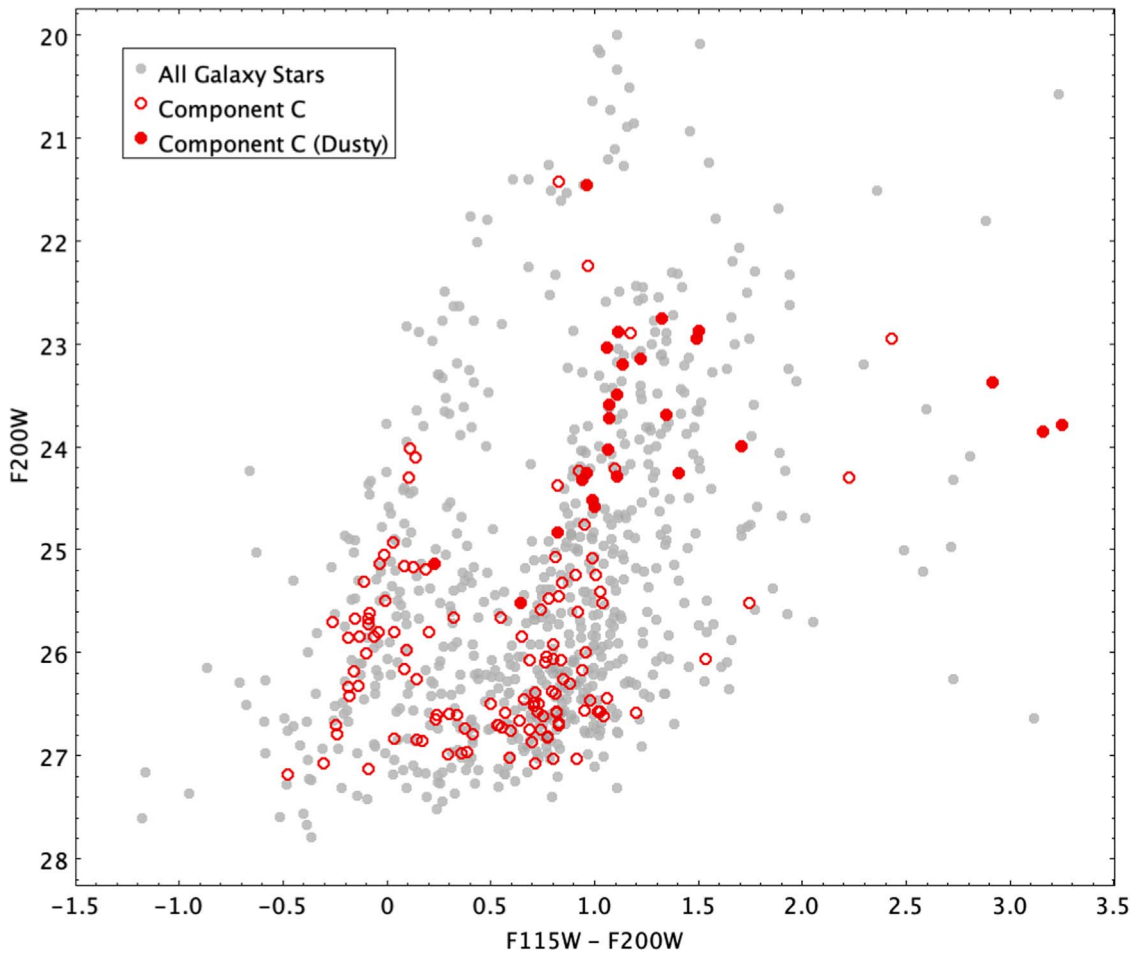


Figure 14. Comparison of the F200W vs. F115W–F200W CMD for stellar sources extracted from Component C (open red circles) against those of I Zw 18’s main body (gray dots). With F200W vs. F115W–F200W ($n = 145$), we are able to recognize the similarities in stellar content between the two systems. A lack of detections on the brighter end of the left branch suggests a dearth of young, hot UMS stars in Component C, while dusty source candidates (red filled circles) appear to predominantly inhabit the bright end of the evolved star branch.

with the literature. In addition, the small number of detected dust-enshrouded source candidates are preferentially located in the bright end of the evolved stars branch.

Acknowledgments

This work is based on observations made with the NASA/ESA/CSA James Webb Space Telescope. The data were obtained from the Mikulski Archive for Space Telescopes (MAST) at the Space Telescope Science Institute, which is operated by the Association of Universities for Research in Astronomy, Inc., under NASA contract NAS 5-03127 for JWST. These observations are associated with program No. 1233. The specific observations analyzed can be accessed via DOI:10.17909/3c1d-6182.

A.S.H. is supported in part by an STScI Postdoctoral Fellowship. A.S.H. extends thanks to Steven R. Goldman for his assistance in clarifying details pertaining to dust production by AGB stars. L.L. acknowledges support from the NSF through grant No. 2054178. O.C.J. acknowledges support from an STFC Webb fellowship. C.N. acknowledges the support of an STFC studentship. M.M. and N.H. acknowledge that a portion of their research was carried out at the Jet Propulsion Laboratory, California Institute of Technology, under a contract with the National Aeronautics and Space Administration (grant No. 80NM0018D0004). M.M. and N.H. acknowledge support















through NASA/JWST grant No. 80NSSC22K0025. K.J. acknowledges support from the Swedish National Space Agency. O.N. was supported by the STScI Postdoctoral Fellowship, and the NASA Postdoctoral Program at NASA Goddard Space Flight Center, administered by Oak Ridge Associated Universities under contract with NASA. G.S.W. acknowledges support of UKSA and STFC. J.B. and P.R. thank the Belgian Federal Science Policy Office (BELSPO) for the provision of financial support in the framework of the PRODEX Programme of the European Space Agency (ESA). NIRCcam and MIRI images created using the *jdaviz* tool (Developers et al. 2023).

Facility: JWST (MIRI, NIRCcam).

Software: *astropy* (Astropy Collaboration et al. 2013, 2018, 2022), *imageio* (Willott 2022), *jdaviz* (Developers et al. 2023), *JHAT* (Rest 2023), *STARBUGII* (Nally 2023), *TOPCAT* (Taylor 2005).

ORCID iDs

Alec S. Hirschauer <https://orcid.org/0000-0002-2954-8622>
 Nicolas Crouzet <https://orcid.org/0000-0001-7866-8738>
 Nolan Habel <https://orcid.org/0000-0002-2667-1676>
 Laura Lenkić <https://orcid.org/0000-0003-4023-8657>
 Conor Nally <https://orcid.org/0000-0002-7512-1662>
 Olivia C. Jones <https://orcid.org/0000-0003-4870-5547>

Giacomo Bortolini  <https://orcid.org/0009-0003-6182-8928>
 Martha L. Boyer  <https://orcid.org/0000-0003-4850-9589>
 Kay Justtanont  <https://orcid.org/0000-0003-1689-9201>
 Margaret Meixner  <https://orcid.org/0000-0002-0522-3743>
 Göran Östlin  <https://orcid.org/0000-0002-3005-1349>
 Gillian S. Wright  <https://orcid.org/0000-0001-7416-7936>
 Ruymán Azzollini  <https://orcid.org/0000-0002-0438-0886>
 Joris A. D. L. Blommaert  <https://orcid.org/0000-0002-5797-2439>
 Bernhard Brandl  <https://orcid.org/0000-0001-9737-169X>
 Leen Decin  <https://orcid.org/0000-0002-5342-8612>
 Omnarayani Nayak  <https://orcid.org/0000-0001-6576-6339>
 Pierre Royer  <https://orcid.org/0000-0001-9341-2546>
 B. A. Sargent  <https://orcid.org/0000-0001-9855-8261>
 Paul van der Werf  <https://orcid.org/0000-0001-5434-5942>

References

- Abazajian, K., Adelman-McCarthy, J. K., Agüeros, M. A., et al. 2004, *AJ*, **128**, 502
- Algera, H. S. B., Inami, H., Oesch, P. A., et al. 2023, *MNRAS*, **518**, 6142
- Alloin, D., Collin-Souffrin, S., Joly, M., & Vigroux, L. 1979, *A&A*, **78**, 200
- Aloisi, A., Clementini, G., Tosi, M., et al. 2007, *ApJL*, **667**, L151
- Aloisi, A., Tosi, M., & Greggio, L. 1999, *AJ*, **118**, 302
- Annibali, F., Cignoni, M., Tosi, M., et al. 2013, *AJ*, **146**, 144
- Astropy Collaboration, Robitaille, T. P., Tollerud, E. J., et al. 2013, *A&A*, **558**, A33
- Astropy Collaboration, Price–Whelan, A. M., Sipőcz, B. M., et al. 2018, *AJ*, **156**, 123
- Astropy Collaboration, Price–Whelan, A. M., Lim, P. L., et al. 2022, *ApJ*, **935**, 167
- Beelen, A., Cox, P., Benford, D. J., et al. 2006, *ApJ*, **642**, 694
- Bernard, J.-P., Reach, W. T., Paradis, D., et al. 2008, *AJ*, **136**, 919
- Bertoldi, F., Carilli, C. L., Cox, P., et al. 2003, *A&A*, **406**, L55
- Blum, R. D., Mould, J. R., Olsen, K. A., et al. 2006, *AJ*, **132**, 2034
- Boothroyd, A. I., & Sackmann, I. J. 1988, *ApJ*, **328**, 653
- Bouchet, P., García-Marín, M., Lagage, P. O., et al. 2015, *PASP*, **127**, 612
- Boyer, M. L., Anderson, J., Gennaro, M., et al. 2022, *RNAAS*, **6**, 191
- Boyer, M. L., McQuinn, K. B. W., Barmby, P., et al. 2015a, *ApJS*, **216**, 10
- Boyer, M. L., McQuinn, K. B. W., Barmby, P., et al. 2015b, *ApJ*, **800**, 51
- Boyer, M. L., McQuinn, K. B. W., Groenewegen, M. A. T., et al. 2017, *ApJ*, **851**, 152
- Boyer, M. L., Srinivasan, S., Riebel, D., et al. 2012, *ApJ*, **748**, 40
- Boyer, M. L., Srinivasan, S., van Loon, J. T., et al. 2011, *AJ*, **142**, 103
- Bradley, L., Sipőcz, B., Robitaille, T., et al. 2022, *astropy/photutils*: v1.5.0, Zenodo, doi:10.5281/zenodo.6825092
- Bressan, A., Marigo, P., Girardi, L., et al. 2012, *MNRAS*, **427**, 127
- Brown, T. M., Heap, S. R., Hubeny, I., Lanz, T., & Lindler, D. 2002, *ApJL*, **579**, L75
- Cannon, J. M., Skillman, E. D., Garnett, D. R., & Dufour, R. J. 2002, *ApJ*, **565**, 931
- Cannon, J. M., Walter, F., Skillman, E. D., & van Zee, L. 2005, *ApJL*, **621**, L21
- Carlson, L. R., Sewilo, M., Meixner, M., Romita, K. A., & Lawton, B. 2012, *A&A*, **542**, A66
- Curtis-Lake, E., Carniani, S., Cameron, A., et al. 2023, *NatAs*, **7**, 622
- Davidson, K., Kinman, T. D., & Friedman, S. D. 1989, *AJ*, **97**, 1591
- de Mello, D. F., Schaerer, D., Heldmann, J., & Leitherer, C. 1998, *ApJ*, **507**, 199
- Dell’Agli, F., Di Criscienzo, M., García-Hernández, D. A., et al. 2019a, *MNRAS*, **482**, 4733
- Dell’Agli, F., Di Criscienzo, M., Ventura, P., et al. 2018, *MNRAS*, **479**, 5035
- Dell’Agli, F., Valiante, R., Kamath, D., Ventura, P., & García-Hernández, D. A. 2019b, *MNRAS*, **486**, 4738
- Developers, J., Averbukh, J., Bradley, L., et al. 2023, *Jdaviz*, v3.8.1, Zenodo, doi:10.5281/zenodo.10420627
- Dicken, Dan, García Marín, Macarena, Shivaiei, Irene, et al. 2024, arXiv:2403.16686
- Dolphin, A. E., Saha, A., Skillman, E. D., et al. 2003, *AJ*, **125**, 1261
- Dufour, R. J., Esteban, C., & Castaneda, H. O. 1996, *ApJL*, **471**, L87
- Dufour, R. J., & Hester, J. J. 1990, *ApJ*, **350**, 149
- French, H. B. 1980, *ApJ*, **240**, 41
- Gardner, J. P., Mather, J. C., Abbott, R., et al. 2023, *PASP*, **135**, 068001
- Garnett, D. R., Skillman, E. D., Dufour, R. J., & Shields, G. A. 1997, *ApJ*, **481**, 174
- Gáspár, A., Rieke, G. H., Guillard, P., et al. 2021, *PASP*, **133**, 014504
- Goldman, S. R., Boyer, M. L., McQuinn, K. B. W., et al. 2019a, *ApJ*, **877**, 49
- Goldman, S. R., Boyer, M. L., McQuinn, K. B. W., et al. 2019b, *ApJ*, **884**, 152
- Gordon, K. D., Bohlin, R., Sloan, G. C., et al. 2022, *AJ*, **163**, 267
- Gordon, K. D., Meixner, M., Meade, M. R., et al. 2011, *AJ*, **142**, 102
- Gruendl, R. A., & Chu, Y.-H. 2009, *ApJS*, **184**, 172
- Habel, N., Nally, C., Lenkić, L., et al. 2024, arXiv:2404.16242
- Herrera-Camus, R., Fisher, D. B., Bolatto, A. D., et al. 2012, *ApJ*, **752**, 112
- Hirschauer, A. S., Gray, L., Meixner, M., et al. 2020, *ApJ*, **892**, 91
- Höfner, S., & Olofsson, H. 2018, *A&ARv*, **26**, 1
- Hunt, L. K., Dyer, K. K., & Thuan, T. X. 2005, *A&A*, **436**, 837
- Hunter, D. A., & Thronson, H. A. J. 1995, *ApJ*, **452**, 238
- Iben, I. J. 1974, *ARA&A*, **12**, 215
- Iben, I. J. 1975, *ApJ*, **196**, 525
- Izotov, Y. I., Chaffee, F. H., Foltz, C. B., et al. 1999, *ApJ*, **527**, 757
- Izotov, Y. I., Foltz, C. B., Green, R. F., Guseva, N. G., & Thuan, T. X. 1997, *ApJL*, **487**, L37
- Izotov, Y. I., & Thuan, T. X. 1998, *ApJ*, **497**, 227
- Izotov, Y. I., & Thuan, T. X. 2004, *ApJ*, **616**, 768
- Izotov, Y. I., & Thuan, T. X. 2016, *MNRAS*, **457**, 64
- James, B. L., Aloisi, A., Heckman, T., Sohn, S. T., & Wolfe, M. A. 2014, *ApJ*, **795**, 109
- Jamet, L., Cerviño, M., Luridiana, V., Pérez, E., & Yakobchuk, T. 2010, *A&A*, **509**, A10
- Janowiecki, S., & Salzer, J. J. 2014, *ApJ*, **793**, 109
- Janowiecki, S., Salzer, J. J., van Zee, L., Rosenberg, J. L., & Skillman, E. 2017, *ApJ*, **836**, 128
- Jones, O. C., Maclay, M. T., Boyer, M. L., et al. 2018, *ApJ*, **854**, 117
- Jones, O. C., McDonald, I., Rich, R. M., et al. 2015a, *MNRAS*, **446**, 1584
- Jones, O. C., Meixner, M., Justtanont, K., & Glasse, A. 2017, *ApJ*, **841**, 15
- Jones, O. C., Meixner, M., Sargent, B. A., et al. 2015b, *ApJ*, **811**, 145
- Jones, O. C., Nally, C., Habel, N., et al. 2023, *NatAs*, **7**, 694
- Jones, O. C., Sharp, M. J., Reiter, M., et al. 2019, *MNRAS*, **490**, 832
- Karakas, A. I. 2010, *MNRAS*, **403**, 1413
- Karakas, A. I., & Lattanzio, J. C. 2003, *PASA*, **20**, 279
- Karakas, A. I., & Lattanzio, J. C. 2014, *PASA*, **31**, e030
- Karakas, A. I., & Lugaro, M. 2016, *ApJ*, **825**, 26
- Kinman, T. D., & Davidson, K. 1981, *ApJ*, **243**, 127
- Kwok, S. 2000, *The Origin and Evolution of Planetary Nebulae* (Cambridge: Cambridge Univ. Press)
- Lattanzio, J. C. 1987, *ApJL*, **313**, L15
- Lattanzio, J. C. 1993, in *IAU Symp. 155, Planetary Nebulae*, ed. R. Weinberger & A. Acker (Dordrecht: Kluwer), 235
- Lebouteiller, V., Heap, S., Hubeny, I., & Kunth, D. 2013, *A&A*, **553**, A16
- Lebouteiller, V., Péquignot, D., Cormier, D., et al. 2017, *A&A*, **602**, A45
- Légrand, F., Kunth, D., Roy, J. R., Mas-Hesse, J. M., & Walsh, J. R. 1997, *A&A*, **326**, L17
- Lelli, F., Verheijen, M., Fraternali, F., & Sancisi, R. 2012, *A&A*, **537**, A72
- Lenkić, L., Nally, C., Jones, O. C., et al. 2024, *ApJ*, **967**, 110
- Lequeux, J., Peimbert, M., Rayo, J. F., Serrano, A., & Torres-Peimbert, S. 1979, *A&A*, **80**, 155
- Lugaro, M., Herwig, F., Lattanzio, J. C., Gallino, R., & Straniero, O. 2003, *ApJ*, **586**, 1305
- Madau, P., & Dickinson, M. 2014, *ARA&A*, **52**, 415
- Madden, S. C., Rémy-Ruyer, A., Galametz, M., et al. 2014, *PASP*, **126**, 1079
- Matsuura, M., Barlow, M. J., Zijlstra, A. A., et al. 2009, *MNRAS*, **396**, 918
- McDonald, I., Boyer, M. L., van Loon, J. T., et al. 2011, *ApJS*, **193**, 23
- McDonald, I., van Loon, J. T., Dupree, A. K., & Boyer, M. L. 2010, *MNRAS*, **405**, 1711
- McQuinn, K. B. W., Boyer, M. L., Mitchell, M. B., et al. 2017, *ApJ*, **834**, 78
- Meixner, M., Gordon, K. D., Indebetouw, R., et al. 2006, *AJ*, **132**, 2268
- Meixner, M., Panuzzo, P., Roman-Duval, J., et al. 2013, *AJ*, **146**, 62
- Motiño Flores, S. M., Wiklund, T., & Eufrazio, R. T. 2021, *ApJ*, **921**, 130
- Nally, C., 2023 StarbugII: JWST PSF Photometry for Crowded Fields, Astrophysics Source Code Library, ascl:2309.012
- Nally, C., Jones, O. C., Lenkić, L., et al. 2024, *MNRAS*, **531**, 183
- Nayak, O., Green, A., Hirschauer, A. S., et al. 2023, *ApJ*, **944**, 26
- Nikolaev, S., & Weinberg, M. D. 2000, *ApJ*, **542**, 804
- Östlin, G. 2000, *ApJL*, **535**, L99
- Östlin, G., & Mouhcine, M. 2005, *A&A*, **433**, 797
- Pagel, B. E. J., Simonson, E. A., Terlevich, R. J., & Edmunds, M. G. 1992, *MNRAS*, **255**, 325
- Perrin, M. D., Sivaramakrishnan, A., Lajoie, C.-P., et al. 2014, *Proc. SPIE*, **9143**, 91433X

- Pilyugin, L. S. 2001, [A&A](#), **374**, 412
- Riebel, D., Srinivasan, S., Sargent, B., & Meixner, M. 2012, [ApJ](#), **753**, 71
- Rieke, M. J., Kelly, D., & Horner, S. 2005, [Proc. SPIE](#), **5904**, 1
- Rieke, M. J., Kelly, D. M., Misselt, K., et al. 2023, [PASP](#), **135**, 028001
- Rieke, G. H., Wright, G. S., Böker, T., et al. 2015, [PASP](#), **127**, 584
- Robitaille, T. P., Whitney, B. A., Indebetouw, R., Wood, K., & Denzmore, P. 2006, [ApJS](#), **167**, 256
- Robson, I., Priddey, R. S., Isaak, K. G., & McMahon, R. G. 2004, [MNRAS](#), **351**, L29
- Sargent, W. L. W., & Searle, L. 1970, [ApJL](#), **162**, L155
- Seale, J. P., Meixner, M., Sewilo, M., et al. 2014, [AJ](#), **148**, 124
- Searle, L., & Sargent, W. L. W. 1972, [ApJ](#), **173**, 25
- Sewilo, M., Carlson, L. R., Seale, J. P., et al. 2013, [ApJ](#), **778**, 15
- Skillman, E. D., & Kennicutt, R. C. J. 1993, [ApJ](#), **411**, 655
- Skillman, E. D., Kennicutt, R. C., & Hodge, P. W. 1989, [ApJ](#), **347**, 875
- Sloan, G. C., Kraemer, K. E., McDonald, I., et al. 2016, [ApJ](#), **826**, 44
- Sloan, G. C., Matsuura, M., Lagarde, E., et al. 2012, [ApJ](#), **752**, 140
- Srinivasan, S., Boyer, M. L., Kemper, F., et al. 2016, [MNRAS](#), **457**, 2814
- Taylor, M. B. 2005, in ASP Conf. Ser. 347, Astronomical Data Analysis Software and Systems XIV, ed. P. Shopbell (San Francisco, CA: ASP), **29**
- Temim, T., Dwek, E., Tchernyshyov, K., et al. 2015, [ApJ](#), **799**, 158
- Thuan, T. X., Lipovetsky, V. A., Martin, J. M., & Pustilnik, S. A. 1999, [A&AS](#), **139**, 1
- van Loon, J. T., Marshall, J. R., & Zijlstra, A. A. 2005, [A&A](#), **442**, 597
- Van Sistine, A., Salzer, J. J., Sugden, A., et al. 2016, [ApJ](#), **824**, 25
- van Zee, L., Westpfahl, D., Haynes, M. P., & Salzer, J. J. 1998, [AJ](#), **115**, 1000
- Ventura, P., Di Criscienzo, M., Carini, R., & D’Antona, F. 2013, [MNRAS](#), **431**, 3642
- Whitelock, P. A., Menzies, J. W., Feast, M. W., & Marigo, P. 2018, [MNRAS](#), **473**, 173
- Whitney, B. A., Sewilo, M., Indebetouw, R., et al. 2008, [AJ](#), **136**, 18
- Wright, G. S., Rieke, G. H., Glaspe, A., et al. 2023, [PASP](#), **135**, 048003
- Wu, Y., Charmandaris, V., Hunt, L. K., et al. 2007, [ApJ](#), **662**, 952
- York, D. G., Adelman, J., Anderson, J. E. J., et al. 2000, [AJ](#), **120**, 1579
- Zwicky, F. 1966, [ApJ](#), **143**, 192